

Determining Future Trajectories of Near-Earth Asteroids From Short Observation Arcs

J.L.Tutt

January 8, 2024

Level 3, Department of Physics, Durham University

This paper investigates the accuracy with which the orbits of near-Earth asteroids can be determined from short observation arcs. After which it assesses the methods used to predict the future trajectories and the hazard of newly discovered asteroids. A selection of both near-Earth and main-belt asteroids were observed from telescopes located in Durham, UK and La Palma, Canary Islands between 5th September and 12th November 2023. Through the method of least squares, we determined our target's orbital elements and achieved values for A866 LA, our target with the shortest arc ($88'0.5'' \pm 0.4''$) of: $a = 2.7699 \pm 0.0002au$, $e = 0.16178 \pm 0.00009$, $i = 5.21339 \pm 0.00005^\circ$, $\Omega = 276.402 \pm 0.005^\circ$, $\omega = 36.99 \pm 0.07^\circ$, $M = 43.44 \pm 0.05^\circ$ all of which lie within 2.86σ of JPL Horizon's accepted values. The NEAs 2008 QY, 2001 NW16 and 1999 SL5 are identified as PHAs based on their calculated diameters and MOIDs, in agreement with literature classifications. We report the closest approaches of each NEA calculated from the geocentric distance over 20,000 days, derive their corresponding positional uncertainties and associated impact probabilities via orbital Monte Carlo. Out of all targets, we predict that 2008 QY will come closest to Earth, reaching $0.04 \pm 0.03au$ on the 3rd October 2039 with an associated impact probability of 9.817×10^{-10} .

1. Introduction

A. Background

Asteroids describe rocky objects in space, predominantly originating from the debris produced during the initial agglomeration of the inner planetary system, Mercury through to Mars [Chodas and Yeomans 1999]. Although most asteroids can be located within the main belt, found between the terrestrial planets and the giant planets [Perna et al. 2013], Near Earth Objects (NEOs) can be formed through gravitational interactions during close encounters with Mars and Jupiter. The resulting orbital modifications, often involving a high eccentricity, can place them on a trajectory passing within 1.3 au of the Sun and therefore within the neighbourhood of Earth's orbit.

Over the last three decades, NEOs have become the subject of both great scientific and political interest, with the mission of discovering over 90% of NEOs with a diameter greater than 140 m by 2020 being initiated into US law by Congress in 2005 under the George E. Brown, Jr (GEB) Act [of Representatives 2005]. Despite failing to meet this target, with only 2/3 of outlined NEOs estimated to have been identified, scientific efforts have continued, as shown by NASA's current development of the NEO Surveillance Mission (NEOSM), a 'space-based IR NEO Survey telescope' [Barbee et al. 2020]. Once operationally mature, the surveys provided by space-based NEOSM and the ground-based Rubin Observatory (formally LSST) will have the potential to achieve the GEB target in under 10 years [Mainzer et al. 2021]. The profound interest these objects have attracted is clearly warranted when considering their simultaneous potential to threaten the extinction of life on earth, provide a keyhole into the formation of the solar system and supply vast reservoirs of valuable resources [Azadmanesh et al. 2023].

B. Hazard of Impact

The consequences of an asteroid impacting the earth could range from 'localized small property damages to catastrophic global extinction events' [Perna et al. 2013]. Therefore, the class of Potentially Hazardous Asteroids (PHAs) are defined as those with an apparent magnitude brighter than 22, suggesting a diameter greater than 140m and a minimum orbital intersection distance (MOID) less than 0.05 au, and thus capable of surviving our atmosphere to produce damage on a regional or even global scale [Li et al. 2019]. Upon comparison with other forms of natural disasters their importance can easily be diminished, with current estimates suggesting impacts from asteroids greater than 1 km in diameter occur every 500,000 years [Harris and D'Abramo 2015], however, historical examples show that the extent of the destruction they threaten justifies the attention they receive. Notably, the most recent

of the great extinctions - the boundary between the Cretaceous and Tertiary periods (the K-T event), occurring 65 million years ago - is widely suspected to be the result of the impact from an asteroid approximately 10km in diameter. An event that resulted in the eradication of half of all living species on earth [Alvarez et al. 1980].

The Tunguska Event of 1908, saw a cosmic body estimated to be 50-80 m in size exploding over the East Siberian taiga 'at an altitude of 6-10 km' [Svetsov 1996] creating a blast footprint of 2000km^2 [Wheeler and Mathias 2019]. Not only showing the damage that impact events from relatively small asteroids can cause but also the recent history of the event confirms its reality within the modern day.

C. Risk Communication

It is the responsibility of astronomers to communicate to the public the realistic threat posed by close encounters and as a result, numerous indexes have been developed. Most notably, the 'Torino Scale' aims to provide an immediate and clear context to the hazard by using 'collision probability and kinetic energy as the principal dimensions for defining the 'hazard space' in which the 0-10 values for the scale are defined' (Figure 1) [Binzel 2000]. Binzel calibrated the scale in a way in which Category 1 represents collision probabilities comparable to the current chance of all size impactors, and therefore Category 0 is not worth public concern. On the other hand, Categories 8-10 represent certain (probability greater than 99%) collisions with dire consequences.

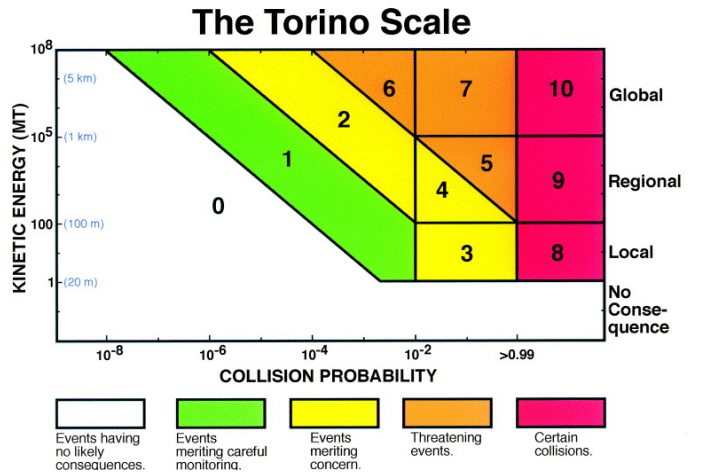


FIG. 1: A diagram showing the Torino Scale's hazard categorisation for celestial bodies based on their kinetic energy (expressed in megatons of TNT) and collision probability.[Binzel 2000]

Within the scientific community the 'Palermo Scale' has greater utility, as not only does it categorise asteroids based on their

impact probability and energy, similar to the ‘Torino Scale’ however also considers quantitatively accounts for the urgency of the threat by considering the possible impact date [Chesley et al. 2002]. This therefore allows objects to be prioritised for additional observations and potential mission planning. With sufficient warning, several proposed remediation techniques could be deployed to avoid future disasters either by the annihilation of the asteroid or displacing it from its trajectory towards Earth. This deflection can be performed by using impulsive methods such as Nuclear Explosions and Kinetic Impactors, or slow-push methods utilising longer-lasting but slower-acting forces [Wang et al. 2023].

D. Scientific and Economic Interest

Concurrently to NEO’s threat to Earth, they are also incredibly valuable to scientific research due to the unique insights they offer into the formation process of the solar system. As relatively untouched remains they contain traces of the ‘chemical mixture of the primordial material from which planets were formed some 4.6 billion years ago’ [Chodas and Yeomans 1999]. The Dawn mission launched in 2007, orbited both 4 Vesta and 1 Ceres, two asteroids complementary in structure with one containing water and the other not, to increase our understanding of both rocky objects typically within the inner solar system as well as icy bodies found in the outer solar system [Russell et al. 2004]. Studying both their geochemistry and geophysics provided evidence for the formation of the solar system in its earliest phases and its subsequent evolution. Scientists have also proposed that asteroids’ historic bombardment of Earth may also be responsible for some of the greatest questions of the 21st century, and have credited them with potentially providing the necessary chemical components for the origin of life and greenhouse gases enhancing Earth’s habitability [Azadmanesh et al. 2023].

Finally, the exploitation of asteroids for the precious resources they contain has become increasingly attractive as the pressure from an increasing world population and Earth’s limited supply of resources accelerates. Asteroids have been found to have higher concentrations of valuable elements, especially platinum group metals (PGMs) which are fundamental in electronics, catalytic converters, and solar cells, than Earth’s crust because most metals sank to the Earth’s core during its early life [Sommariva 2015]. Studies quantify this, finding NEOs commonly contain 10-20 times the grade of PGMs than open pits operating in South Africa, and further support the financial viability of asteroid mining by suggesting ‘10% of Near-Earth Asteroids (NEAs) are energetically more accessible than the moon’ [Sonter 2006].

E. Aims of Paper

In all three cases discussed, it is essential that NEOs’ orbits can be accurately mapped, for their position with respect to Earth to be precisely determined over time. Whether this is to be able to predict future collisions with Earth, and if so, positions at which preventative methods can be best implemented, or calculating close approaches to Earth for which scientific observation and mining missions are likely to be most financially feasible. As a result of the limited accuracy of positional measurements and a finite number of observations over a restricted orbital arc, there is a finite precision to which an asteroid’s orbit can be determined. Consequently, there is an intrinsic uncertainty to which future trajectories can be predicted.

This paper investigates the accuracy with which the orbital characteristics of Near-Earth Asteroids (NEAs) can be determined over short observation periods and arcs; a crucial calculation when an asteroid is first discovered to quickly determine its future trajectory and whether it poses an immediate or future threat. The importance of rapid accurate orbital determination from short observation periods can be shown by the 19m diameter

‘Chelyabinsk asteroidal impactor’, which entered Earth’s atmosphere above Russia without warning on the 15th February 2013 and is estimated to have released an energy equivalent to 500 kilotons of trinitrotoluene (TNT) [Brown et al. 2013].

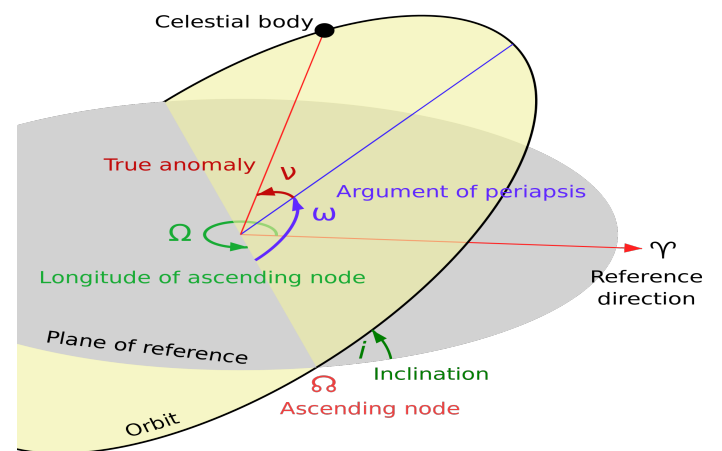


FIG. 2: A 3-D representation of the six Keplerian elements used to define an orbital plane (shown in yellow) with respect to the reference plane (shown in grey) and the phase/position of a celestial body within said orbit. [Commons 2023]

Asteroids’ orbits can be defined using the six orbital (Keplerian) elements centred on the sun, where the size and shape of the orbit are defined by the parameters called the Eccentricity (e) and the Semi-major axis (a). The orientation of the orbit plane within space is described by the Euler angles called the Inclination (i), the Longitude of the ascending node (Ω), and the Argument of Periapsis (ω) [Shin et al. 2015]. The True anomaly (v) describes the position of the body within its orbit at a specific epoch, however this paper commonly refers to the Mean anomaly (M), which is a unit converted from v such that it varies linearly with time. NEAs are commonly categorised into ‘Amors’, ‘Apollos’ and ‘Atens’ defined on their Semimajor axis (a) as well as the distances at which they are closest and furthest from the sun, referred to as their Perihelion distance (q), and Aphelion Distance (Q) respectively [Binzel et al. 2002].

Class	Semi-Major Axis(a) Range [Au]	Perihelion(q)/Aphelion(Q) Range [Au]	Proportion of total population
Amors	$a \geq 1$	$1.017 < q < 1.3$	~45%
Apollos	$a \geq 1$	$q < 1.1017$	~45%
Atens	$a < 1$	$Q > 0.983$	~8%

TABLE I: Categories of Near Earth Asteroid

This paper aims to:

1. Determine how accurately asteroids’ positions can be measured from ground-based telescopes during short observation periods and arcs.
2. Investigate the precision to which an asteroid’s orbital characteristics can be determined from a limited number of observational measurements.
3. Be able to establish whether an asteroid poses a sufficient threat (PHA) to warrant further investigation.
4. Model the asteroid’s future trajectory to calculate the dates and locations of closest approaches to Earth for future mission planning.
5. Calculate an asteroid’s probability of impacting Earth during a close approach through the uncertainty in future positions.

In Section 2, we discuss the procedures undertaken to determine the celestial coordinates from ground-based observation. The

methods used to generate orbital elements from our observations are described in Section 3. Section 4 sees the application of our determined orbits to predict future close approaches and impact probabilities of near-earth asteroids. Finally, Section 5 discusses the limitations of our results and the paper's future application to wider science.

2. Observations

A. Primary Data Collection

This paper analyses data obtained by five of Durham University's telescopes, DRACO2, East-16, Far-East-20, West-14 located in Durham, UK and the remotely operated 0.5m telescope (pt5m) on La Palma, The Canary Islands. The CCD images were taken throughout the observing window from 25th September to 12th November 2023.

Telescope	Diameter	f-ratio	Mount	Camera	Filters Available	Pixel scale ("/pixel)
West-14	14"	10	Meade LX200	QSI 683	C, B, V, R, E	0.91
East-16	16"	10	10micronGM 2000	Moravian G3-16200	C, B, V, g, r	0.93
DRACO2	14"	10	10micronGM 2000	QSI 683	C, B, V, R, E	0.983
Far-East 20	19.7"	10	10micronGM 2000	Moravian C4-1600	C, B, V, R, I, Ha, OIII	1.07
Pt5m	19.7"	10	Astelco NTM-500	QSI 532ws	U, B, V, R, I	0.28

TABLE II: Technical Specifications of the Telescopes, Mounts and Cameras used

The NEOs subject to the investigation include 1999 SL5, 2001 XR31 2002 NW16 and 2008 QY. This paper also studies a handful of Main Belt asteroids such as A854 EB, A852 VA, A866 LA, and A861 GB, as their inclusion provides several experimental advantages. Due to the variable weather in Durham, the primary observing location, the opportunity to take consistently spaced images within a short observation arc on a NEO (eg. 2 images every night for a week) was unlikely to occur. Alternatively, main belt asteroids' slower tracks across the sky would provide an equivalent observation arc over the whole observation period, shown by their tracking profile within Figure 3. Therefore, the study of main belt asteroids allows us to replicate the scenario in which a previously undetected asteroid is rapidly approaching Earth and thus investigate the accuracy with which its threat could be immediately assessed from multiple images over a short arc (10 images within one night).

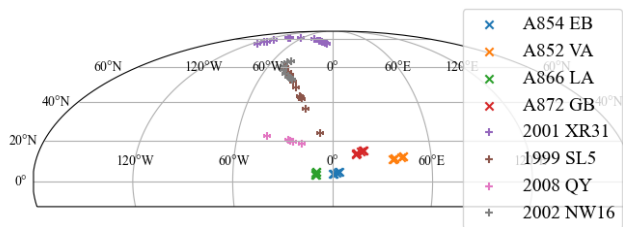


FIG. 3: The observed locations of all studied asteroids on the celestial sphere during the observation window of this paper, sketching out each target's recorded observation arc.

Furthermore, due to their consistently brighter apparent magnitudes, they are not only more frequently observable during periods of high atmospheric seeing and low-density clouds, but also observable for greater windows of time. On the other hand, due to the NEO's smaller size and greater variation in distance from Earth during the observation window, they were often only observable for a limited period within the window. For example, we found that the minimum observable brightness with the equipment used corresponded to an apparent magnitude of 18.8. Thus as the main belt asteroid A852 VA's apparent magnitude only ranged from 9.9 to 10.9 during the observation period, it was observable the whole time, compared to the

NEO 2008 QY, which was only observable from 1st October to 7th November 2023 as its apparent magnitude ranged from 14.7 to 27.0.

This study heavily relies on the accuracy of positional measurements and therefore careful attention was given when focusing images to minimise their full-width half maxima (FWHM) so that they were limited by atmospheric seeing. The FWHM is a constant for all point sources within the image however dimmer sources appear narrower in comparison to background radiation. Our experimental equipment usually resulted in typical FWHM values of ~ 2.5 arcseconds. Exposure times were carefully re-selected for each target during every observing period to account for differences in the apparent magnitude, seeing, moon phase, telescope, filter and position within the sky (zenith angle) in an effort to maximise the signal-to-noise ratio (SNR) without exceeding the CCD's linearity limit. The focus on astrometry rather than photometry resulted in the clear (C) filter being used on all images, apart from those taken by the pt5m which used the visual (V) filter. Additionally, 5 exposures were taken for each target during each observing session, this not only allowed for the tracking of the object over the night sky to help identify it, but also allowed the 'best image' to be chosen for processing, ie. where the target asteroid is furthest from other stars in a region of relatively low noise, as well as including the highest number of catalogued stars.

B. Astrometry

To convert an image's pixel coordinates (x and y) to the celestial coordinates (right ascension (RA) and Declination (DEC)), which describe a location on the celestial sphere, an astrometric calibration was applied. This process was performed by the Graphical Astronomy and Image Analysis (GAIA) tool in which a transformation is determined through the comparison between the image and an astrometric reference catalogue. This paper uses the Gaia Catalogue of Nearby Stars, a 'large well-characterised catalogue' of 331,312 objects within 100pc of the sun [Smart et al. 2021]. The uncertainty in the computed astrometric position, the random projection error σ_{proj} , is derived from the covariance matrix produced by the transformation [Barghini et al. 2019]. To minimise this error, the image with the highest number of identifiable catalogued stars was chosen when possible as this increased the number of data points used during the calibration. We typically achieved values of ~ 0.18 arcseconds.

The target asteroids were identified by tracking their movement across multiple exposures relative to stationary background stars, as well as overlaying the reference star catalogue, to reveal unaccounted-for sources. Once identified, the precise location of the object within the image's frames is identified using GAIA's pick object function, which fits a two-dimensional Gaussian Point Spread Function (PSF) to the light source defined by Equation (1) [Raab 2002].

$$I_{(x,y)} = H \times e^{-\frac{(x-x_0)^2 + (y-y_0)^2}{2\sigma_{psf}^2}} + B \quad (1)$$

The intensity $I(x,y)$ defined by the PSF in Equation (1) is formulated from 5 key coefficients $x_0, y_0, H, \sigma_{psf}, B$. Key to this paper, the positional coordinates (x_0, y_0) describe the source's location within the frame and were converted into celestial coordinates using the transformation derived earlier from the astrometric calibration. The height of the Gaussian fit (H) determines the total area under the PSF which is equivalent to the total flux plus the background signal (B). Finally, σ_{psf} describes the width of the Gaussian PSF directly corresponding to the FWHM, through Equation (2).

$$\sigma_{psf} = \frac{FWHM}{2\sqrt{2\ln 2}} \quad (2)$$

Clearly, a bright point source with a high signal-to-noise ratio (SNR) will be able to have a more accurate PSF mapped to it than a faint, low SNR source. The positional error of a source is therefore dependent upon its SNR. Raab[2002] suggests that the relationship between the observed magnitude and SNR for given telescope setups can be easily determined and in turn, related to the overall error in position, σ_{pos} , shown in Equation (3).

$$\sigma_{pos} = \frac{\sigma_{psf}}{SNR} = \frac{FWHM}{2\sqrt{2\ln 2} \times SNR} \quad (3)$$

Ideally, aperture photometry would be performed on every observation to determine its unique SNR and FWHM in order to calculate the overall positional error, σ_{pos} , for each measurement, however this was implausible due to time constraints. Instead, aperture photometry was limited to a representative observation (with seeing ~ 3.5 arcseconds) from Durham's Draco 2 telescope on 15th October 2023 and the σ_{pos} for a sample of catalogued stars ranging in magnitude (9-18) was calculated. This image was chosen as most observations throughout our data collection were taken using the Draco 2 telescope and the slightly higher-than-average seeing provided a conservative estimate of the true error.

We hypothesised that the relationship between V-band magnitude, m_v and σ_{pos} could be accurately modelled by the exponential function shown in Equation (4). Performing a reduced chi-squared, χ^2 , optimisation to the fit, we achieved a χ^2 value of 1.057 suggesting a very strong correlation. The resultant parameters were calculated to be $A = 4.3 \times 10^{-7} \pm 9 \times 10^{-8}$ and $B = 0.693 \pm 0.01$ and the suitability of the fit can be seen visually in Figure 4.

$$\sigma_{pos} = A e^{B \times m_v} \quad (4)$$

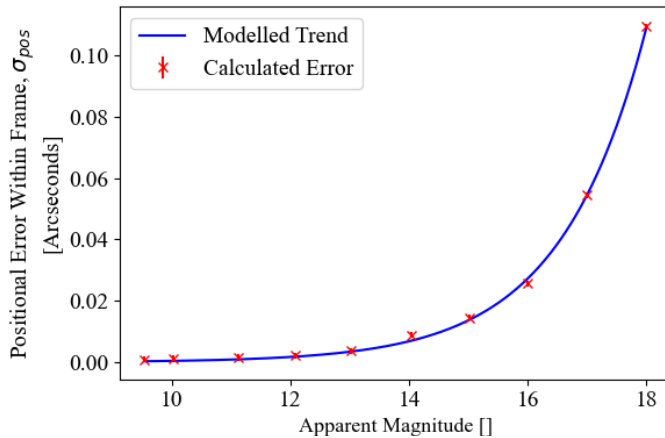


FIG. 4: The random positional uncertainty in the light sources centre within the frame, σ_{pos} , across a range of apparent magnitudes, calculated from aperture photometry for a conservative image taken from the Draco 2 telescope with seeing $3.5''$. The graph has an exponential relationship modelled with χ^2 analysis overlaid to show their agreement.

This relationship was then used to determine the positional error, σ_{pos} , for each of our targets' measurements by cross-referencing the precise epoch of the observation with JPL's Horizons database to extract the given V-Band magnitude and apply Equation (4). This model's viability is reduced when used on observations from different experimental setups and/or extreme exposure lengths. Upon reflection, separate models could have been created for all telescopes and commonly repeated exposure lengths.

The overall error of the celestial coordinates is a combination of both the projection error σ_{proj} and the PSF's positional error σ_{pos} and is therefore calculated by adding them in quadrature which was performed individually for each positional measurement. From Figure 4, it can be seen that as the magnitude increases,

σ_{pos} becomes much more significant and comparable to σ_{proj} . Therefore, although negligible for our brighter main-belt asteroids, it is an important factor for our dimmer, closer targets.

C. Comparison with JPL Horizons

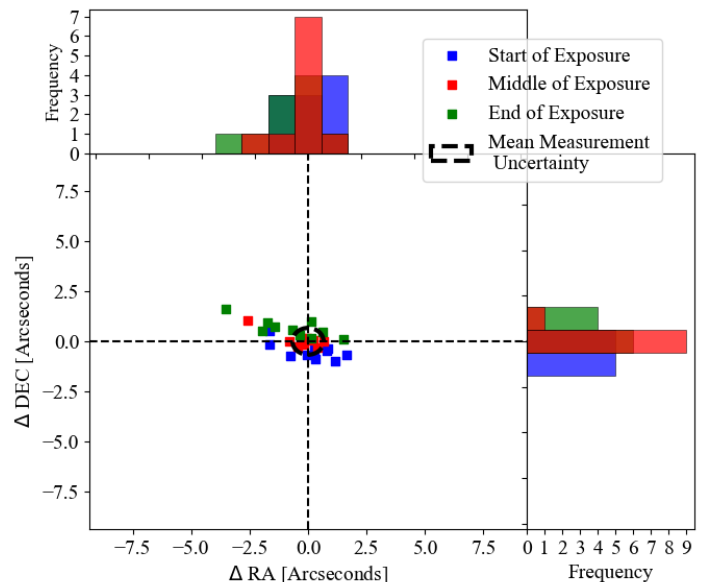


FIG. 5: The deviation of all our calculated celestial coordinates, RA and DEC, from JPL horizons' predictions for 2002 NW16. The deviations are calculated using three comparative JPL data points at the start, middle and end of each observation, to show potential errors created from incorrect time stamps during orbital fitting. Histograms are created using 15 bins across each dimension to show the data points' distribution and help identify systematic errors.

The accuracy of positional measurements achieved for each target asteroid was then verified by comparing them to the JPL Horizons' predicted position at the time the exposure was taken. JPL Horizons' database provides highly accurate ephemerides for a catalogue of solar system bodies calculated using years of observations and advanced modelling. Figure 5 shows the deviations of the achieved celestial coordinates from JPL's predictions for asteroid 2002 NW16. The average error across all observations of 2002 NW16 is all shown for comparison with the spread of the data. Figures of the other target's deviations can be found within the Section 8 C. The figure shows the difference in the positional measurement compared to three different values within JPL's database; the position predicted at the start, middle and end of each exposure. This is a detail we initially overlooked as we began by associating all our positional measurements with the time at the start of the exposure.

Upon analysis of this graph, using the exposure's start time causes a systematic error unaccounted for by our measurements' uncertainties, shown by none of the deviations from JPL's data falling within the average uncertainty of the measured positions. However, when using the time at the middle of the exposure a clear agreement can be seen due to a majority (7 out of 10) of observations falling within the mean uncertainty. This systematic error can be concluded to be a result of the movement of asteroids during the exposure, as the trend in position errors from start to end directly correlates to their track across the sky shown in Figure 3. As shown by our data and reasoned by CCDs integrating light sources over the whole exposure, the centre of the fitted PSF is therefore most representative of the position of the light source in the middle of the exposure.

This can be further supported by the significantly greater systematic error in measurements of NEO asteroids compared to those within the main belt. This can be shown quantitatively as the maximum deviation of a NEO found was $8.50''$ (2001 XR31) compared to MB's maximum of $0.31''$ (A852 VA). This is likely a result of the longer exposure time (typically 90 seconds) required to observe the dim NEO targets combined with their faster movement

across the sky, resulting in a greater overall change in position over the exposure. As a result, we later use the time in the middle of the exposure time when performing orbital determination calculations to remove this error and increase accuracy.

The histograms of the distribution of deviations in RA and DEC show that once the systematic error has been accounted for, the errors in positional measurements are centred at zero and randomly distributed on either side. The random error remaining can still be seen to be more significant for NEO targets, as shown by the red histograms' wider spread. This is once again likely a result of the dimmer targets moving faster over a longer exposure resulting in far less accurate PSF being able to be modelled, and thus far greater uncertainty in resulting position. However overall, our positional measurements show a high level of agreement with JPL Horizons' predictions and have sufficient accuracy to justify basing further analysis on them.

3. Orbital Elements Determination

A. Find Orb

To convert our set of positional measurements into a set of orbital elements, Project Pluto's 'Find Orb' orbit determination software was utilised. Find Orb allowed us to perform a least-squares fit by varying parameters to minimise the deviation between our measured celestial coordinates and those predicted by the modelled orbit. Keplerian elements, although efficient at representing orbits in 3D space, have flaws during optimisation calculations, for example as inclination, i , of an orbit tends to zero the argument of the periaxis (ω) becomes ill-defined. Therefore, the parameters used to perform the optimisation are the state vectors x, y, z, v_x, v_y, v_z opposed to the Keplerian elements outputted in an effort to avoid mathematical singularities. To increase the accuracy of the optimisation, we declared the calculated uncertainties in each of our input celestial coordinates, which allowed each observation to be weighted within the calculation proportionally.

When using open-access software it is important to verify the validity of its results by quantifying the accuracy to which it can be trusted. This was done by using documented orbital elements from JPL Horizons to calculate a given celestial body's ephemeris for a short period. These calculated positions at regular intervals were inputted into Find Orb and the resulting elements were compared back to those from JPL. By using data points determined directly from orbital elements, their error is effectively zero therefore the error from input data is isolated and the results expose the accuracy of the software itself. To closely simulate the data inputs used in our experiment, the target '2008 QY' was chosen, with positions calculated at 23:59 every 2 days between 08th October 2023 to 14th March 2024. We investigated the trend between the number of data points used in the method of least-squares and the accuracy to which the orbit can be determined by varying the number of inputs from 4 up to 96, shown in Figure 6,

With both axes on logarithmic scales, we can see the clear relationship that the fractional error decreases as the number of observations increases. One key characteristic of this graph is the sudden temporary decrease in all elements' fractional error, down to values as low as $\sim 1 \times 10^{-8}$ for the eccentricity, when calculated based on 14 data points. However, as this is a singular data point it is likely an anomalous coincidental agreement between Find Orb and the true values. Furthermore, beyond 70 data points, although there is still a degree of random variation, the fractional error appears to have reached a lower limit suggesting more observations no longer provide greater accuracy. For our target celestial bodies, we achieved an average of 10 observations, thus by interpolating the graph we can estimate an average fractional uncertainty on our elements of 8.78×10^{-5} . This allowed us to produce a lower limit on the un-

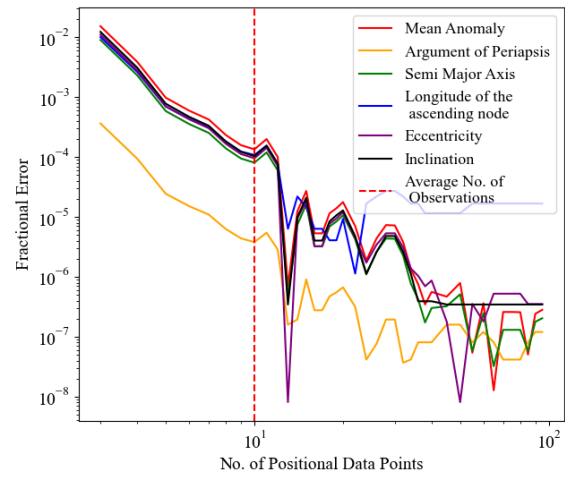


FIG. 6: The fractional error of Find Orb's outputted elements from celestial coordinates calculated directly from accepted orbital elements of 2008 QY from JPL Horizons plotted against the number of input data points provided. The data points are distributed every 2 days between 8th October 2023 to 14th March 2024. The average number of observations achieved for a given target in this paper, 10, is shown.

certainty of outputted orbital elements, as although Find Orb may be able to model an orbit that has a very high agreement with our observations and thus suggests very low error, there is a limit to the accuracy of the software's calculation. Overall, even when only 4 data points are used, Find Orb calculates orbital elements to within an average fractional error of 9.71×10^{-3} which is sufficiently accurate to justify its use for the analysis of our primary data.

For each target asteroid, we used Find Orb to derive the orbital elements for 00:00 on the 12th of November 2023. The elements calculated are associated with a specific epoch, as an asteroid's orbit can vary over time due to gravitational perturbations and other non-gravitational effects such as solar radiation pressure, discussed in Section 5 C. This specific epoch was chosen as it marks the end of our observational period and therefore is the latest date for which our data can support the orbital elements calculated.

B. Orbital Elements' Uncertainties

Although Find Orb produces uncertainties for the calculated orbital elements derived from the covariance matrix associated with the least squares fit, this paper employs two alternative methods to compute the uncertainties directly; 'Observational Monte Carlo' and 'Jackknifing'. This is not only to reduce the reliance on third-party software but also as the covariance ellipsoid produced from short observation arcs cannot be trusted to represent the true uncertainty of the orbit [Milani et al. 2005].

The virtual-observation Markov-chain Monte Carlo method referred to as 'Observational Monte Carlo', outlined by Muinonen et al. [2012], 'virtual observations' by randomly applying Gaussian noise to each pair of angular celestial coordinates, the distribution of which is defined by their unique uncertainties. The corresponding 'virtual orbital elements' are calculated by performing a least-squares optimisation on the set of virtual observations. This process is then repeated for many sets of virtual observations to create a spectrum and associated probability distribution function (PDF) of potential orbital elements. This paper iterates this process 1000 times for each target.

Jackknife resampling was used as an alternative method of estimating the uncertainty in our orbital elements, a universal and robust technique especially helpful for variance estimation and bias identification. The method creates a set of 'jackknife replicates', X_1, \dots, X_n , by removing one observation at a time in turn from the sample of n and determining the orbital elements by performing a least-squares fit on the remaining $(n-1)$ observations. The mean and the standard deviation of the replicates were calculated as shown

in Equation (5) [Sawyer 2005].

$$\bar{X} = \frac{1}{n} \sum_{i=1}^n X_i \quad (5a)$$

$$\sigma_{jk} = \sqrt{\frac{\sum_{i=1}^n (X_i - \bar{X})^2}{n-1}} \quad (5b)$$

This allows biases in the data set to be evaluated by comparing the average of the ‘jackknife replicates’ orbital elements and the original orbital elements calculated from the full sample size. A large difference in these two values would mean that the jackknife replicates are not evenly distributed about the original value and therefore suggest that one or more positional measurements are distorting the results and thus erroneous. This could either be the result of one or more positional values being incorrectly calculated, or their estimated uncertainty being too low, thus assigning them greater weighting than justified. This feature of jackknifing makes it advantageous when dealing with a small number of observations over small observation arcs as it accurately represents the effect of positional error on the overall uncertainty.

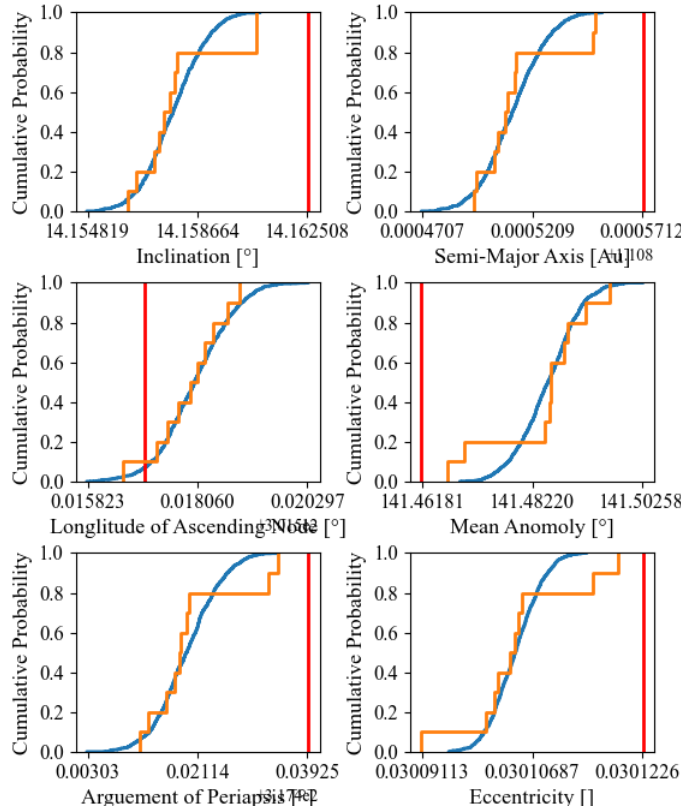


FIG. 7:

The cumulative probability distributions of each element created through jackknife (orange) and observational Monte Carlo analysis (blue) for 2002 NW16 are plotted against one another for comparison. The accepted value of each element given by JPL Horizons (red) is also shown.

The comparison between the orbital elements’ distributions from jackknife residuals and observational Monte Carlo for Target 2002 NW16 can be seen in Figure 7 (similar graphs for other targets can be found within the Section 8 D). The JPL Horizons’ accepted orbital elements are also shown to provide qualitative context for biases seen in some targets. The key difference between the distributions for 2002 NW16 is their ‘smoothness’ which is simply a result of the number of data points defining them. Observational Monte Carlo is defined by 1000 data points and is only limited by computational processing power whereas jackknifing is defined by 10 and is limited by the number of observations. Despite this, their overall structure is in strong agreement and thus the probability functions they describe are very similar, suggesting that

the jackknife residuals are distributed randomly about the mean value and follow a similar PDF to observational Monte Carlo.

On the other hand, for targets such as 1999 SL5, 2008 QY and A854 EB (see Section 8 D) there is an anomalous set of orbital elements created by one of the jackknife replicates, breaking down the agreement between the two methods of determining orbital uncertainty. Although easy to assume that that anomalous replicate’s omitted data point is responsible for the error and should be removed, further study of 1999 SL5’s distribution in comparison with JPL’s tabulated result shows that the replicate’s orbital elements have similar deviations from the accepted values than other data points. Deeper analysis is therefore required to conclude the causes of any bias and exclude data points, which would likely require a greater number of observations than available.

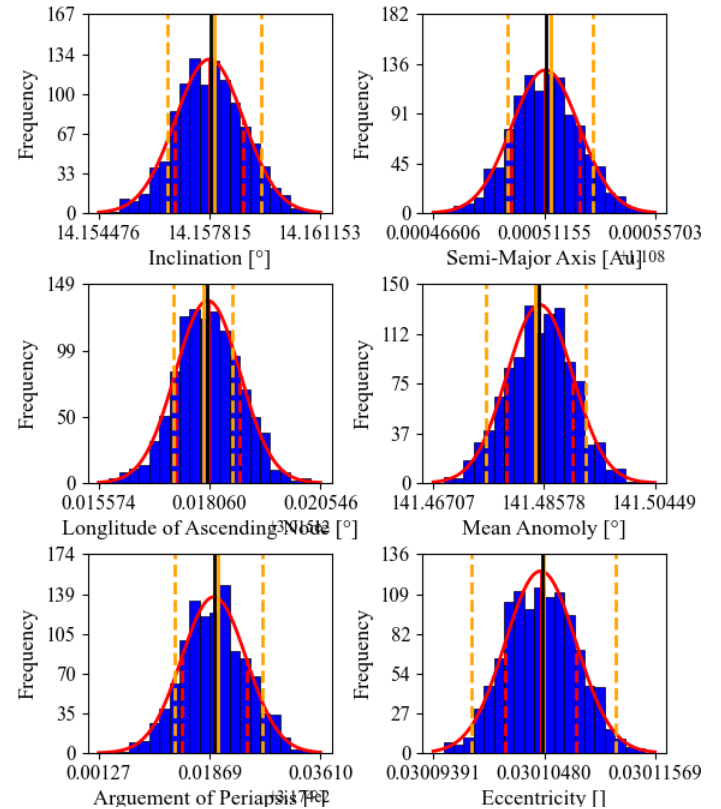


FIG. 8: 2002 NW16’s determined orbital elements from Find Orb using the full observational sample (black), the jackknife mean (orange solid), and the mean from the Gaussian distribution (red solid) fitted to observational Monte Carlo’s results (blue) are plotted against each other. The one-sigma error given by Monte Carlo (red dashed) and jackknifing (orange dashed) are also marked.

The resultant mean orbital elements and their estimated one-sigma errors from both methods can be seen in Figure 8 as well as the parameters achieved by Find Orb from the full set of positional measurements (see Section 8 E for other target’s uncertainty comparisons). The uncertainty achieved through observational Monte Carlo was quantified by modelling a normal distribution to the data. The suitability of this model for the PDF can be seen through the very strong agreement with the histograms, showing that by adding Gaussian noise to positional measurements (inputs) we achieved a Gaussian distribution of fitted orbital elements (outputs), similar to that of ‘Orbital Monte Carlo’. For the case of 2002 NW16, shown in Figure 8, we can see a negligible difference between the three methods of determining the mean ‘value’ for orbital elements suggesting bias is not an issue. Furthermore, we can see that the standard deviation calculated through jackknifing consistently provides a more conservative estimate of error than that achieved from observational Monte Carlo, an average across all elements of 1.41 times greater, a trend seen across all targets.

For a target with a bias present, such as 1999 SL5, a key similarity is the results from observational Monte Carlo are still

negligibly different from Find Orb's results from the full observation sample. Also, the spread in the Monte Carlo distribution and thus the standard deviation it achieves remains consistent (similar magnitude) when compared to similar targets (NEA or MB) with lower biases suggesting it is unable to account for this error. On the other hand, we can see a clear difference between Find Orb's result and the jackknife mean as expected, and importantly the jackknife standard deviation is much greater and therefore the bias is reflected in the estimated uncertainty. This is shown by the jackknifing's standard deviation now being on average 4.46 times greater than that provided by observational Monte Carlo. Target 2008 QY can be seen to have an uncharacteristically high disagreement between both the orbital elements' means and uncertainties for the two statistical methods. This is a result of the small number of observations, 5, available due to the short period it was observable. Therefore, each observation has a much greater effect on the orbit modelled, resulting in a much higher uncertainty. Once again, we can see jackknifing is able to account for this and provides much more representative values for the uncertainties, showing them all being an order of magnitude greater than other NEAs. As a result of its consistently more conservative values as well as its ability to reflect the identified biases, we chose the jack-knife's one-sigma error to define the uncertainty in our orbital parameters during further analysis. Finally, our orbital elements' values themselves are most accurately represented by the results outputted directly from Find Orb when calculated from the maximal set of positional measurements.

C. Effect of observation arc

As a focus of this paper, it is important to investigate the effect of the arc length on our orbital elements and their uncertainties through the comparison between the results from Near Earth Asteroids (longer arc lengths) and those from Main Belt Asteroids (shorter arc lengths). Table III and Table IV show the calculated orbital elements from representative targets, 2002 NW16 and A866 LA respectively, as well as their accepted values from JPL Horizons (see Section 8 F for all other targets tabulated results). Within our experiment we observed arcs for 2002 NW16 and A866 LA of $12^\circ 7' 5.1'' \pm 0.6''$ and $0^\circ 88' 0.5'' \pm 0.4''$ respectively. Through the comparison of the figures showing the uncertainties from both methods employed (Figure 8), as well as the one-sigma errors of the jackknife method within the results tables, we can see that as the observed arc length for a target decreases, the spread in the orbital elements' probability functions increases and thus so does their uncertainty. This can be seen to affect the one-sigma values for both observational Monte Carlo and jackknifing proportionally to one another, resulting in the absolute uncertainty values for orbital elements typically being $\sim 1\text{-}2$ orders of magnitude greater for MB asteroids than NEAs. This can be explained by method of least-squares being more sensitive over short arcs as they represent much smaller proportions of the overall orbit and therefore the possible results extrapolated from the region have a much greater spread. Thus, as our achieved positional measurements have relatively constant uncertainties, they have much higher significance within short observation arcs and their effect on orbital elements when varied through observational Monte Carlo or removed during jackknifing are much higher.

Finally, we evaluate our calculated orbits by comparing them and their uncertainties with JPL Horizons' data. In the above tables, the absolute difference between our results and the accepted values given by JPL (the error) is given, as well as the error in the context of the uncertainties' one-sigma error bars. As expected, we conclude that we can better determine the orbit of targets with longer observation arcs, as the absolute difference between our value and JPL's are typically an order of magnitude smaller for NEAs than MBs. However, when reviewing the agreement between the values in the context of our determined uncertainties, we can see that the accepted

Elements	Find Orb	JPL Horizons	Absolute Difference	Difference (one-Sigma errors)
<i>Eccentricity [</i>]	0.030105 ±0.000003	0.030123	0.000018	5.21
<i>Semi Major Axis [AU]</i>	1.10851 ±0.00001	1.10857	0.00006	4.27
<i>Inclination [°]</i>	14.158 ±0.001	14.163	0.005	4.56
<i>Argument of Periapsis [°]</i>	317.420 ±0.005	317.439	0.020	3.92
<i>Longitude of the ascending node [°]</i>	301.518 ±0.001	301.517	0.001	1.40
<i>Mean Anomaly [°]</i>	141.485 ±0.006	141.462	0.023	4.19

TABLE III: Orbital elements for 2002 NW16

Elements	Find Orb	JPL Horizons	Absolute Difference	Difference (one-Sigma errors)
<i>Eccentricity [</i>]	0.16178 ±0.00009	0.16205	0.00027	2.83
<i>Semi Major Axis [AU]</i>	2.7699 ±0.0002	2.7696	0.0003	1.73
<i>Inclination [°]</i>	5.21339 ±0.00005	5.21346	0.00007	1.28
<i>Argument of Periapsis [°]</i>	36.99 ±0.07	36.79	0.19	2.65
<i>Longitude of the ascending node [°]</i>	276.402 ±0.005	276.415	0.013	2.60
<i>Mean Anomaly [°]</i>	43.44 ±0.05	43.56	0.12	2.61

TABLE IV: Orbital elements for A866 LA

values typically lie $\sim 1\text{-}2$ sigma error bars from our calculated elements for MBs whereas for NEAs this is much greater, typically $\sim 4\text{-}6$ sigma error bars away. This suggests that although we are able to more accurately determine the orbital elements for longer arc targets, we have been able to better estimate the uncertainty in shorter arc targets. It is important to consider the fact that by seemingly having underestimated the uncertainty in our NEAs, the spread of 'virtual asteroids' in 3D space in future analysis is likely greater than calculated.

There are two targets which are shown to have uncharacteristically high disagreements with accepted values, 2001 XR31 (NEA), with orbital elements being off by ~ 8 sigma error bars and A854 EB's (NEA) orbital elements being off by ~ 5.5 sigma error bars, suggesting additional sources of error. For A854 EB this is likely a result of the potential erroneous data point forming a bias revealed by the jackknife mean, as discussed earlier. Whereas in the case of 2001 XR31, it likely traces back to the discussion of the significant random error in its positional measurements due to its long exposure time combined with fast track across the sky, shown by its residual plot. Overall, we have been able to determine the orbital elements to a sufficient level of accuracy to estimate future trajectories and close approaches.

D. Categorisation of Orbits

The orbital elements determined allow each NEO to be assigned to a category in Table I. Furthermore the Minimum Orbital Intersection Distance (MOID) with Earth, which describes the distance between the closest points on the bodies' orbits, can be calculated. The MOID provides an estimate of potential closest approach between celestial bodies which in turn corresponds to impact probabilities. To determine whether a given body qualifies as a Potential Hazardous Asteroid (defined previously), its diameter is also required. This paper uses Find Orb to provide a rough estimate of the target bodies' diameters from their observed apparent magnitude and assumes an albedo (reflection coefficient) of 10%. This calculation provides a very approximate value which should not be used for any further analysis, but due to the achieved diameters being far above

the threshold of 140m they are sufficient to identify PHAs.

Target	Type	Determined MOID [AU]	JPL Horizons MOID [AU]	Diameter [m]
2008 QY	Apollo (PHA)	0.0309	0.0306	~670
2002 NW16	Amor	0.0673	0.0671	~790
2001 XR31	Apollo (PHA)	0.0251	0.0253	~1600
1999 SL5	Apollo (PHA)	0.0244	0.0252	~1300

TABLE V: The calculated MOIDs, diameter for each NEO and their resultant classifications.

This paper, based on the MOIDs and diameters shown in Table V concludes targets 2008 QY, 2001 NW16 and 1999 SL5 are PHAs. All classifications are in agreement with JPL Horizons. Although the MOID of an asteroid provides the shortest distance from Earth possible on its current orbit, it does not consider the relative motion of the bodies within their orbits. Thus further investigation is required to find its non-hypothetical closest approaches by accounting for its position as well as Earth's within their respective orbits over time.

4. Close Approaches

A. Cartesian Orbital Representation

By converting our orbit's Keplerian elements into Cartesian coordinates, we can visualise their heliocentric trajectories within 3D space. Figure 9 shows the orbits of our studied Near Earth Asteroids within the solar system, as well as Earth's for comparison (see Section 8 G for the orbits for the Main Belt asteroids). These are shown within the ecliptic plane, the orbital plane created by the earth around the sun. The uncertainty in each target's Cartesian position during its orbit is represented by the thickness of the lines and derived through 'orbital Monte Carlo' analysis. Similar to observational Monte Carlo, orbital Monte Carlo repeatedly adds random Gaussian noise to a series of parameters each with individual uncertainties and analyses the distribution of the results achieved from the varied inputs. However, instead of creating 'virtual observations', a set of 'virtual asteroids' are created for each target by varying their orbital elements separately. Within Figure 9, 1000 virtual asteroids have been created for each target and their 3-D orbits overlaid on each other.

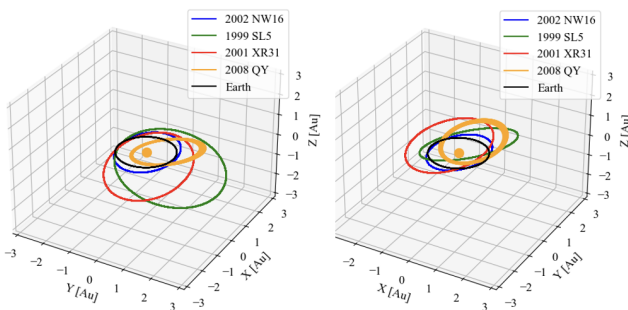


FIG. 9: A 3-D Cartesian representation of the heliocentric orbits of our target NEAs within the solar system ecliptic plane. The uncertainty in the orbits' trajectories calculated through orbital Monte Carlo is represented by their thickness. The Sun's fixed position at the origin and the Earth Orbit are also shown.

The thickness of 2008 QY's line shows the large range of orbits possible due to its comparatively high uncertainties in the orbital elements as a result of the method of least-squares being performed on a small range of observations. We have previously discussed the likely underestimation of the uncertainties in all NEAs' orbits through comparison with JPL Horizons' accepted values. As a result, the thickness of all lines and range in possible orbits is likely larger than shown. One limitation to this representation of the

orbital uncertainty is that the initial thickness of the lines must be sufficient so that it can be seen, however, this creates a lower limit for the visualized uncertainty in the orbit. This means that orbits below a threshold are indistinguishable and comparisons are invalid. This is the case for the plot of main belt asteroids, which appear to have constant uncertainties (thickness) for all orbits.

B. Geocentric Distance

In the next section, the open-access Python library, Poliastro, was implemented to aid the calculation of the geocentric distance (distance from Earth) of targets over time. This is done by simultaneously calculating the heliocentric positions of the Earth and a given target at a specific epoch, through its orbital elements defined at 00:00 on the 12th of November 2023, and determining the difference between them. This was calculated for all NEA targets from the 12th of November 2023 for the following 20,000 days (~ 55 years), every 24 hours at 00:00. The MB targets' distance from Earth is not investigated as their orbit within the main belt makes their close approaches insignificant. From this, the three closest approaches to Earth are calculated computationally by identifying the minimum turning points within the graph and determining the three with the shortest geocentric distance and their corresponding date and time.

The data was only calculated 20,000 days into the future as it relied on the assumption that orbital elements were invariant, however, factors such as gravitational perturbations and solar radiation pressure, discussed in Section 5 C, are likely to distort the orbit over time and therefore further extrapolation would require these effects to be modelled and accounted for. Furthermore, uncertainties in orbital elements, especially the semi-major axis, affect the period of orbits and thus both the errors in close approach date and position increase with time, meaning results from any further forward in time would have inadequately large uncertainties.

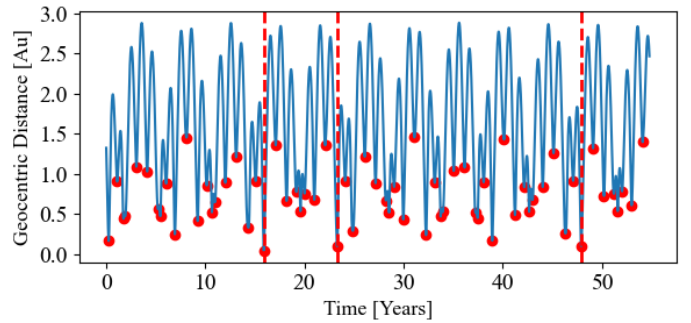


FIG. 10: The geocentric distance of 2008 QY over 20,000 days from the 12th November 2023 is shown (blue). All minimum turning points are marked (red dot) and the three closest approaches are highlighted (red dashed).

Figure 10 shows the plot of the geocentric distance of 2008 QY over time, with minimum turning points marked and the three closest approaches identified (see Section 8 H for plots of other NEA targets). Comparing the graphs for different targets, we can see that some asteroids such as 2002 NW16 have very cyclical and periodic relationships whereas targets such as 2008 QY show much more random and variable patterns, although rough repeating trends can be identified. For 2002 NW16 this is likely due to the similarities of its orbital elements with Earth (with a semi-major axis of 1.10851 ± 0.000001 au and eccentricity 0.030105 ± 0.000003) resulting in a simple and regularly repeating pattern, however in the case of 2008 QY with an eccentricity of 0.588 ± 0.001 , its orbit is considerably different to that of the earth resulting in a much more irregular trend.

C. Positional Uncertainty

The uncertainties in the closest approaches' positions were calculated through orbital Monte Carlo. As described before,

multiple virtual asteroids are created for each target through the addition of random noise to their orbital elements. For each virtual asteroid, the Cartesian geocentric positions were calculated for the specific dates of its closest approach discovered above. This was performed for each of the NEA targets' three closest approaches using 1000 iterations, creating a spread of possible positions in 3D space at each specific epoch. To quantify the positional uncertainty, we mapped a 3-D Gaussian probability function and determined the one-sigma error bars for each dimension x, y and z. The uncertainties in each dimension were propagated to achieve an overall uncertainty in the distance from the Earth.

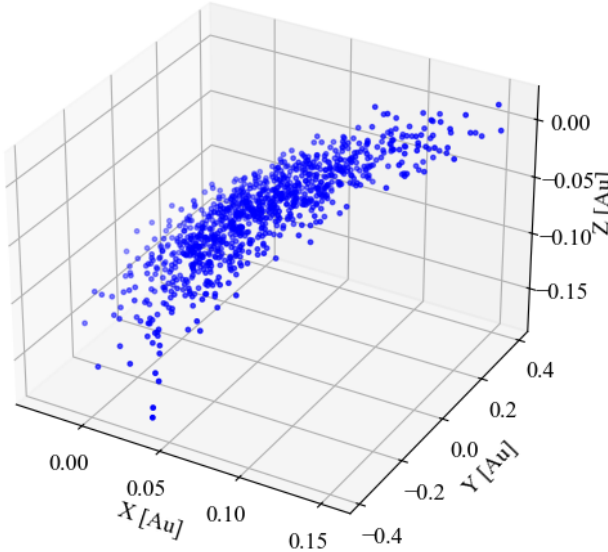


FIG. 11:

The geocentric positions of 1000 virtual asteroids of 2008 QY on the 18th of February 2047 are shown, calculated via orbital Monte Carlo from elements defined on the 12th of November 2023.

Figure 56 of 2008 QY's closest approach on the 18th February 2047 shows the 3-D spread of virtual asteroids at that specific epoch (see Section 8J for similar diagrams of each target NEA's closest approach). We can see the 3-D spread in position appears to be in the shape of a curved ellipsoid or 'bananoid' as suggested by Vavilov [2020]. This curvature is seen to correspond to the nominal orbit and therefore is a result of the differences in virtual asteroids' mean motion and period. This would suggest that as time is extrapolated further, the differences in the asteroid's phases along the orbit would further increase causing greater uncertainty in the true position. (See Section 8J for visualisations of the derivation of the uncertainty in each dimension and the suitability of modeling a Gaussian probability function through the strong agreement between the histogram and the achieved model, examples can be found for each target NEA's closest approach).

Date	X [Au]	Y [Au]	Z [Au]	Total Distance [Au]
3 rd October 2039	-0.01 ±0.03	0.03 ±0.06	-0.03 ±0.01	0.04 ±0.03
18 th February 2054	0.04 ±0.03	0.1 ±0.1	-0.07 ±0.03	0.05 ±0.05
29 th September 2071	-0.01 ±0.03	0.10 ±0.06	0.00 ±0.01	0.10 ±0.04

TABLE VI: 2008 QY's top three closest approaches

Table XIX shows the three closest approaches for 2008 QY over the next 20,000 days in chronological order (see Section 8I for tables of all target NEAs closest approaches). The uncertainties in this target's positions are ~2-3 orders of magnitude greater than the other targets due to the high uncertainties in its orbital elements.

However, across all targets, we are unable to find a clear correlation between positional uncertainty and the length of time in the future as predicted. This may be a result of only having three data points available for each target across a relatively short period (~55 years), however, it could imply there is an alternative dominant uncertainty creating the distinctive distribution of virtual asteroids.

Although the method used provides a valid way of determining the uncertainty in the position of a celestial body at a specified epoch, there is an error in applying this method directly to determine the uncertainty in the closest approach distance. This is because due to small variations in virtual asteroids' orbits, they all reach their unique closest approach at different times. To more accurately apply orbital Monte Carlo to determine the uncertainty, the geocentric distance for each virtual asteroid should be mapped over time and each closest approach position and time recorded. Similarly to before, a 3-D probability function can then be mapped to the new spread in positional measurements for the closest approaches but additionally, the variation in the timing of the closest approach can be analysed to provide an uncertainty in the time. This was not performed due to being highly resource-intensive and requiring substantial processing power.

Target	Date	Closest Approach Total Distance [Au]
2008 QY	3 rd October 2039	0.04 ± 0.03
2002 NW16	29 th October 2040	0.13314 ± 0.00009
2001 XR31	29 th October 2055	0.24534 ± 0.00003
1999 SL5	8 th October 2074	0.3877 ± 0.0001

TABLE VII: The closest approach of each NEA

Table VII shows each target's closest approach (over the next 20,000 days) and the time it occurs.

D. Impact Probability

The impact probabilities of NEAs were calculated for each closest approach epoch via the positional 3-D Gaussian probability function, by integrating over the region where the geocentric distance is less than the Earth's radius. This is accurately approximated through the product of all three dimensions' separately considered probabilities. For all targets other than 2008 QY we achieve zero probabilities.

Date	Impact Probability
3 rd October 2039	2.129x10 ⁻¹⁰
18 th February 2054	9.817x10 ⁻¹²
29 th September 2071	2.986x10 ⁻¹⁰

TABLE VIII: Impact probabilities during 2008 QY's closest approaches

Table VIII shows the impact probabilities for 2008 QY during its calculated closest approaches. Although still very small ($\sim 1 \times 10^{-10}$), its non-zero probability result is due to it having both the closest approaches to Earth and its much higher uncertainty in positional predictions.

The statistical validity of our achieved impact probabilities can be quantified by investigating the error in the probability itself. Vavilov and Medvedev (2014) proposed that the error, σ_{MC} , in the impact probability, P_{MC} , is dependent on the number of virtual asteroids, m , used to define the probability function through the relationship shown in Equation (6).

$$m = \frac{P_{MC}(1-P_{MC})}{\sigma_{MC}^2} \quad (6)$$

Thus, to be able to calculate an impact probability of order $\sim 1 \times 10^{-10}$ with 50% certainty, it would require the orbital propagation of 4×10^{10} virtual asteroids, resulting in it being a very time-consuming and computationally demanding method. The accuracy level we achieve through the simulation of 1000 virtual asteroids for our probabilities is $\sim 3 \times 10^{-7}$ which is 3 orders of magnitude greater than the probability itself. Therefore, our calculations were performed on insufficiently large statistical bases (VA cloud) to be able to attain a reliable value. In general, the orbital Monte Carlo method is likely unsuitable for determining low-impact probabilities.

5. Discussion

A. Observations and Astrometry

The accuracy of primary observations and their statistically derived uncertainties underpin the reliability of results from all further analyses. Being able to reduce measurements positional post-fit residuals, would allow them to be weighted much more highly within orbital least-squares fitting providing greater certainty in the fitted orbital parameters.

There are many sources of both random and systematic errors, some of which are intrinsic to asteroid astrometry and out of the hands of the observer. Above we highlighted the greater uncertainty in our faint sources (NEAs) due to the difficulty in mapping their PSFs with a lower signal-to-noise ratio. This is because the noise created by the sky background, read-out noise, and the CCD's thermal noise is much more comparable to that of the light source's signal and, therefore, can influence the modelling of a light source's central position (x,y) randomly. Another source of random error is the 'shot noise', which is created due to the random rate of photon emission from a source and thus the disparity between the distribution captured by a finite exposure time and the true overall distribution [Owen 2000]. Often these could be reduced by increasing the exposure time, however, due to the high relative motion of our asteroids across the sky this would introduce a greater source of error due to asteroid trailing. Instead, multiple images could be taken and stacked, as random errors from photon statistics are inversely proportional to the square root of the number of observations. As stacking images of fast-moving targets across a similar period would also cause trailing effects, ideally multiple identical telescopes in the same location would be used to simultaneously take images of the target and these could be processed.

Secondly, our astrometric measurements from Durham University's on-site telescopes are significantly limited by the atmospheric conditions. Both the spread of light sources (atmospheric seeing) and their apparent central position (atmospheric refraction) are affected because of random atmospheric turbulence, from fluctuations in air temperature and density along its path. The main way this source of uncertainty can be reduced is the use of observatories with better seeing, often placed on coastal mountain tops which allows them to be higher in altitude than common temperature inversion layers and within stable high-pressure systems caused by the prevailing wind's laminar flow from the ocean. Our observation from the La Palma Observatory (pt5m) typically provided much lower seeing (shown in Section 8 B) however its access was limited during the observing window. Another way to further increase the accuracy of astrometric measurements is to increase the angular resolution of the telescope by increasing its diameter, however this would require sufficiently low atmospheric seeing for it to not be the limiting factor.

The conversion to our celestial coordinates in the equatorial reference frame, J2000, is based on the calibration to a star

catalogue. Carpino et al. [2003] discovered biases within star catalogues suggesting the presence of systematic errors within our results. It is important to consider the significance of the bias created by the 'Gaia Catalogue of Nearby Stars' used in this paper and establish whether debiasing techniques are required for our observations. However, in comparison to the other sources of error, Gaia's astrometric data is found to have a standard uncertainty in right accession of 0.374 milli-arcseconds and declination of 0.335 milli-arcseconds for magnitude 20 stars [Lindegren et al. 2021] and therefore the bias present within this modern catalogue is negligible.

To apply the techniques in determining orbital elements and impact probabilities from short observation arcs presented in this paper to the international effort of meeting the GEB target, they must be combined with an autonomous asteroid detection system. Telescopes such as the LSST, with wide fields of view, will be able to scan large portions of the sky and compare exposures over time to identify moving targets for further investigation. Additionally, these techniques can be applied to space-based missions. The planned NEOMIR will overcome a significant number of the limitations created by the reliance on optical ground-based observations, as is the case in this paper. As Conversi et al (2023) highlight by placing the NEOMIR at the L1 Lagrange point and observing in the IR spectrum, it will be able to observe asteroids at very low solar elongations from Earth which are not visible from ground-based observations, such as the asteroid responsible for the Chelyabinsk impact. Additionally, one of the many other advantages is due to the lack of atmosphere, it will achieve much higher resolutions and therefore more accurately be able to determine positional measurements.

B. Orbit Determination

This paper identifies a clear correlation between the accuracy of our targets' calculated orbits and their observation arc (shown visually in Figure 3). However, the basis of this paper is to investigate how accurately we can rapidly determine the future trajectory of newly discovered celestial bodies. Therefore, although effective, increasing the observation arc (period) of a given target reduces the method's applicability to gaining an initial assessment of its threat and potential for observing and mining missions. Alternatively, the uncharacteristically high uncertainty in 2008 QY's orbit in comparison to other NEOs supports the theory that the density of observations within a given period also affects the accuracy of our results. A greater number of observations would not only allow the method of least-squares to be performed on a greater number of data points but also allow us to further investigate the biases shown during the jackknife resampling. The major limitations for the frequency of our observations were poor weather and only being able to observe the target in optical wavelengths at night.

The use of radar observations would allow more frequent observations by exploiting radio waves and microwaves as they can penetrate clouds and are invariant to background optical light (ie. the time of day). Furthermore, [Giorgini et al. 2009] suggests that using high precision 'radar astrometry can reduce trajectory uncertainties several orders of magnitude' for newly discovered objects further supporting their use. It would also provide a greater level of detail for the dimensions, shape and speed of each NEA and thus also be able to help quantify its potential threat within the Torino or Palermo Scale. Finally, Owen [2000] highlights the systematic error created by the assumption that the centre of light determined from our optical observation directly corresponds to the centre of mass required for orbital fitting, an error not present in the analysis of radar astrometry.

The apparent underestimation in the uncertainty of our NEOs' orbital elements from jackknifing resulted in parameters typically being ~ 5 one-sigma errors from accepted values given by JPL Horizons. It is important to investigate alternative methods for

orbital determination and error analysis in an effort to be able to more accurately quantify the range of possible orbits that can be derived from our observations. Virtanen [2001] presents the method of ‘statistical ranging’ for asteroids with a small number of observations over short arcs which allows the examination of ‘orbital element phase space for possible orbits even in the most indeterminate cases’. The method creates a set of all trial orbits based on two observations from the sample (typically the first and last) and then tests each orbit’s validity by comparing them to all observations. If the trial orbit reproduces all data points with sufficient accuracy it is added to a set of ‘possible orbits’. To determine statistical ranging’s possible merits over the ‘full step’ least-squares fitting used, further analysis is required as our observation arcs are theoretically sufficiently long to justify our original choices.

C. Close Approaches

Our calculations of future positions from orbital elements defined on the 12th of November 2023 assume they are constant; however, gravitational and non-gravitational effects can distort the orbit over time. Firstly, due to the solar system’s complicated web of gravitational interactions, asteroids are continuously perturbed, these effects can cause significant alterations in the trajectory of an asteroid, especially during close encounters with large bodies,. This is more common for asteroids with large eccentricity, as they cross a greater number of planetary orbits. To quantify the gravitational effects on the orbital elements, we used Find Orb to integrate the position of our asteroid forward in time accounting for gravitational forces from all planets and major asteroid perturbers such as Ceres, Pallas and Vesta. From this the change in orbital elements over time was determined. Across all our target NEAs, we achieve a maximum fractional change of 0.0013 in the Semi Major axis and 0.050 in the eccentricity which occurred in 2002 NW16. Therefore, the change in orbital elements is insignificant in comparison to their initial uncertainties and therefore accounting for them over this time frame does not provide any major advantage (Graphs showing the fractional change in orbital elements over time can be found within the Section 8 K).

The solar radiation pressure (SRP) significance must also be considered due to asteroids’ relatively high surface area to volume ratio thus the exchange of momentum between electromagnetic radiation and the object can create tangible forces and torques on the body. Vokrouhlicky et al. [2015] identify the importance of factoring in non-gravitational effects due to their potential to ‘produce measurable orbital changes over decades’, namely the Yarkovsky and YORP Effects. The Yarkovsky effect is the consequence of the lag between the absorption of incoming radiation and the resulting increase in the intensity of thermal radiation emission on a rotating body. Thus, a net force is created by the difference in absorption and emission directions and depending on the object’s rotational axis, the semi-major axis of the orbit will either increase or decrease. The YORP effect, the less significant of the two, causes changes to a body’s angular momentum due to the absorption and diffuse reflection of solar radiation. These effects were unable to be modelled accurately due to the lack of knowledge of the target’s rotation rate, axis, surface structure and albedo. However, by only projecting the geocentric distance ~ 55 years into the future, it once again will have had a negligible effect on the orbits in comparison to the virtual asteroids’ spread from orbital uncertainty. Further extrapolation would require these non-gravitational effects to be accurately modelled due to their cumulative properties.

We have previously mentioned the limitations in our determination of the positional uncertainty of asteroids’ closest approach due to each Monte Carlo virtual asteroid arriving at slightly different times. Chodas and Yeomans [Yeomans and Chodas 1994] propose a solution to this by forming an impact plane, ‘by projecting the error ellipsoid into the plane perpendicular to the velocity vector of

the Earth relative to the object’ thus removing the element of time.

We determined the impact probability from the error ellipsoid’s Gaussian probability function by integrating over the region within the earth’s radius at the time of closest approach. However, the radius in which an impact would occur is more accurately defined by the larger ‘gravitational radius’, dependent upon the impactor velocity. This larger radius is because Earth’s gravity is capable of attracting a potential impactor as it passes on a near-miss trajectory. Therefore, our calculated impact probabilities consistently provide an underestimation of the true probability, and future calculations of impact probability should account for this.

6. Conclusion

This paper’s focus is to propose a procedure for orbital determination of newly discovered asteroids to be able to model their future trajectories from short observation arcs. Aiming to assist future decisions in either mission requirements to prevent possible impacts with Earth or the suitability of targets for scientific observation and mining as well as the best opportunities to do so.

From our primary observations, we have been able to accurately calculate the celestial coordinates of our target asteroids over time through astrometry calculations. We obtain higher uncertainties in our NEO objects due to their fainter apparent magnitudes and faster tracks across the sky causing a less accurate PSF to be modelled. Despite this when compared to accepted values provided by JPL Horizons, the majority of data points fall within the intrinsic uncertainty in the equipment used. The most effective method discussed for increasing the accuracy of our positional measurements would be decreasing atmospheric seeing by using high-altitude coastal telescopes, such as La Palma or space-based observatories.

We then modelled orbits to these primary observations of our MB and NEA targets, using a least-squares method, to produce sets of orbital elements. Overall for the longer arc NEA targets, we achieved lower absolute errors between JPL’s accepted values and ours, however, we attained a more realistic representation of the elements’ uncertainties in our MB targets. Regardless, we are still able to accurately determine the orbital elements of our lowest arc object, A866 LA, which has an observation arc of just $88^\circ 0.5'' \pm 0.4''$, supporting the application of our method to rapidly assess the threat and scientific potential of a newly discovered asteroid.

Our orbital elements allowed us to classify our NEOs and determine their need for further investigation through their associated MOID. In agreement with JPL, we were able to classify 2008 QY, 2001 NW16 and 1999 SL5 as Apollos as well as PHAs and 2001 XR31 as an Amor. We went on to calculate close approaches and impact probabilities for our NEOs over the next 20,000 years and were able to provide the predicted times and positions of the three closest passes to Earth. But further study of their dimensions, structures and potential impact velocities is required to quantify their threat on scales such as the Torino and Palermo Scale. These downfalls could be fulfilled by radar observations due to its extensive range of advantages discussed. Future applications of the procedures demonstrated in this paper to the GEB target, will require their use alongside all-sky surveys scanning for the movement of light sources across exposures, such as LSST.

7. Acknowledgements

I am grateful for the support and encouragement of scientific curiosity offered by Professor Mark Swinbank and Professor Alastair Edge throughout this process. I would also like to thank Claire Greenwell and Kathryn Barrett for numerous helpful discussions and assistance during the laboratory sessions. Finally, this paper would not be possible without the tireless work of my

laboratory partner, Thomas Walker.

References

- Luis W. Alvarez, Walter Alvarez, et al. Extraterrestrial cause for the cretaceous-tertiary extinction. 208(4448):1095–1108, 1980. ISSN 0036-8075, 1095-9203. doi: 10.1126/science.208.4448.1095. URL <https://www.science.org/doi/10.1126/science.208.4448.1095>.
- M. Azadmanesh, J. Roshanian, and M. Hassanalian. On the importance of studying asteroids: A comprehensive review. 142:100957, 2023. ISSN 0376-0421. doi: <https://doi.org/10.1016/j.paeosci.2023.100957>. URL <https://www.sciencedirect.com/science/article/pii/S0376042123000738>.
- Brent W Barbee et al. Future spacecraft missions for planetary defense preparation. 2020.
- D. Barghini, D. Gardiol, et al. Astrometric calibration for all-sky cameras revisited. 626:A105, 2019. ISSN 0004-6361, 1432-0746. doi: 10.1051/0004-6361/201935580. URL <https://www.aanda.org/10.1051/0004-6361/201935580>.
- Richard P Binzel. The torino impact hazard scale. 48(4):297–303, 2000. ISSN 00320633. doi: 10.1016/S0032-0633(00)00064. URL <https://linkinghub.elsevier.com/retrieve/pii/S0032063300000064>.
- Richard P Binzel et al. Physical properties of near-earth objects. 255(271), 2002. Publisher: this volume. Univ. of Arizona, Tucson.
- P. G. Brown, J. D. Assink, et al. A 500-kiloton airburst over chelyabinsk and an enhanced hazard from small impactors. 503(7475):238–241, 2013. ISSN 0028-0836, 1476-4687. doi: 10.1038/nature12741. URL <https://www.nature.com/articles/nature12741>.
- Mario Carpino, Andrea Milani, and Steven R. Chesley. Error statistics of asteroid optical astrometric observations. 166(2):248–270, 2003. ISSN 00191035. doi: 10.1016/S0019-1035(03)00051-4. URL <https://linkinghub.elsevier.com/retrieve/pii/S0019103503000514>.
- Steven R. Chesley et al. Quantifying the risk posed by potential earth impacts. 159(2):423–432, 2002. ISSN 0019-1035. doi: <https://doi.org/10.1006/icar.2002.6910>. URL <https://www.sciencedirect.com/science/article/pii/S0019103502969101>.
- P Chodas and D Yeomans. Orbit determination and estimation of impact probability for near earth objects. 1999. Publisher: Citeseer.
- Wikimedia Commons. File:orbit1.svg — wikimedia commons, the free media repository, 2023. URL <https://commons.wikimedia.org/w/index.php?title=File:Orbit1.svg&oldid=823141887>. [Online; accessed 4-January-2024].
- Jon D. Giorgini et al. Radar astrometry of small bodies: detection, characterization, trajectory prediction, and hazard assessment. 2009. URL <https://hdl.handle.net/2014/45703>. Section: Tue Sep 01 00:00:00 UTC 2009.
- Alan W. Harris and Germano D’Abramo. The population of near-earth asteroids. 257:302–312, 2015. ISSN 00191035. doi: 10.1016/j.icarus.2015.05.004. URL <https://linkinghub.elsevier.com/retrieve/pii/S0019103515002067>.
- Miao Li, Yukun Huang, and Shengping Gong. Assessing the risk of potentially hazardous asteroids through mean motion resonances analyses. 364(5):78, 2019. ISSN 0004-640X, 1572-946X. doi: 10.1007/s10509-019-3557-5. URL <http://link.springer.com/10.1007/s10509-019-3557-5>.
- L. Lindegren, S. A. Klioner, et al. Gaia early data release 3: The astrometric solution. 649:A2, 2021. ISSN 0004-6361, 1432-0746. doi: 10.1051/0004-6361/202039709. URL <https://www.aanda.org/10.1051/0004-6361/202039709>.
- Amy Mainzer, P. Abell, et al. The future of planetary defense in the era of advanced surveys. 53(4), 2021. doi: 10.3847/25c2cfba7af878. URL <https://baas.aas.org/pub/2021n4i259>.
- Andrea Milani et al. From astrometry to celestial mechanics: Orbit determination with very short arcs: (heinrich k. eichhorn memorial lecture). 92(1):1–18, 2005. ISSN 0923-2958, 1572-9478. doi: 10.1007/s10569-005-3314-7. URL <http://link.springer.com/10.1007/s10569-005-3314-7>.
- Karri Muinonen, Mikael Granvik, et al. Asteroid orbital inversion using a virtual-observation markov-chain monte carlo method. 73(1):15–20, 2012. ISSN 00320633. doi: 10.1016/j.pss.2012.07.016. URL <https://linkinghub.elsevier.com/retrieve/pii/S0032063312002103>.
- House of Representatives. Nasa authorization act of 2005., 2005. URL <https://www.congress.gov/109/plaws/publ155/PLAW-109publ155.pdf>.
- William M. Owen, Jr. Error sources in asteroid astrometry. 00:58165, 2000. URL <https://ui.adsabs.harvard.edu/abs/2000STIN...0058165O>. ADS Bibcode: 2000STIN...0058165O.
- D. Perna, M. A. Barucci, and M. Fulchignoni. The near-earth objects and their potential threat to our planet. 21(1):65, 2013. ISSN 1432-0754. doi: 10.1007/s00159-013-0065-4. URL <https://doi.org/10.1007/s00159-013-0065-4>.
- Herbert Raab. Detecting and measuring faint point sources with a CCD. pages 1–12. Citeseer, 2002.
- C.T. Russell, A. Coradini, et al. Dawn: A journey in space and time. 52(5):465–489, 2004. ISSN 00320633. doi: 10.1016/j.pss.2003.06.013. URL <https://linkinghub.elsevier.com/retrieve/pii/S0032063303002277>.
- S Sawyer. Resampling data: Using a statistical jackknife. 2005.
- Yuchul Shin, Seyoung Yoon, Yongmyung Seo, Ho Jin, and Jongho Seon. Radiation effect for a CubeSat in slow transition from the earth to the moon. 55(7):1792–1798, 2015. ISSN 02731177. doi: 10.1016/j.asr.2015.01.018. URL <https://linkinghub.elsevier.com/retrieve/pii/S027311771500054X>.
- R. L. Smart, L. M. Sarro, et al. Gaia early data release 3: The gaia catalogue of nearby stars. 649:A6, 2021. ISSN 0004-6361, 1432-0746. doi: 10.1051/0004-6361/202039498. URL <https://www.aanda.org/10.1051/0004-6361/202039498>.
- Andrea Sommariva. Rationale, strategies, and economics for exploration and mining of asteroids. 13(1):25–42, 2015. ISSN 1477-7622, 1557-2943. doi: 10.1080/14777622.2015.1014244. URL <http://www.tandfonline.com/doi/abs/10.1080/14777622.2015.1014244>.
- Mark Sonter. Asteroid mining: key to space economy. 6:2009, 2006.
- V. V. Svetsov. Total ablation of the debris from the 1908 tunguska explosion. 383(6602):697–699, 1996. ISSN 0028-0836, 1476-4687. doi: 10.1038/383697a0. URL <https://www.nature.com/articles/383697a0>.
- Dmitrii E Vavilov. The partial banana mapping: a robust linear method for impact probability estimation. 492(3):4546–4552, 2020. ISSN 0035-8711, 1365-2966. doi: 10.1093/mnras/stz3540. URL <https://academic.oup.com/mnras/article/492/3/4546/5681408>.
- J Virtanen. Statistical ranging of asteroid orbits. 154(2):412–431, 2001. ISSN 00191035. doi: 10.1006/icar.2001.6592. URL <https://linkinghub.elsevier.com/retrieve/pii/S0019103501965923>.
- D. Vokrouhlický, W. F. Bottke, et al. The yarkovsky and YORP effects. 2015. doi: 10.48550/ARXIV.1502.01249. URL <https://arxiv.org/abs/1502.01249>. Publisher: arXiv Version Number: 1.
- Yirui Wang et al. Intelligent selection of NEO deflection strategies under uncertainty. 72(7):2676–2688, 2023. ISSN 02731177. doi: 10.1016/j.asr.2022.08.086. URL <https://linkinghub.elsevier.com/retrieve/pii/S027311772008389>.
- Lorian F. Wheeler and Donovan L. Mathias. Probabilistic assessment of tunguska-scale asteroid impacts. 327:83–96, 2019. ISSN 00191035. doi: 10.1016/j.icarus.2018.12.017. URL <https://linkinghub.elsevier.com/retrieve/pii/S0019103518304676>.
- D. K. Yeomans and P. W. Chodas. Predicting Close Approaches of Asteroids and Comets to Earth. 1994. URL <https://ui.adsabs.harvard.edu/abs/1994hdte.conf..241Y>. Conference Name: Hazards Due to Comets and Asteroids Pages: 241 ADS Bibcode: 1994hdte.conf..241Y.

8. Appendix

A. Observation Log

Date	Time (UTC)	Telescope(s)	Band	Exposures Taken	1999 SL5	2001 XR31	2002 NW16	2008 QY	A866 LA	A854 EB	A872 GB	A852 VA
25 September 2023	21:00-21:30	Draco 2	C	22	X	X	X					
29 September 2023	20:00-20:30	Draco 2	C	16	X	X						
1 October 2023	20:15-20:45	Draco 2	C	14	X	X	X					
5 October 2023	19:30-20:00	Draco 2	C	12	X	X						
9 October 2023	20:00-20:45	Far-East 20	C	27	X			X				
14 October 2023	20:00-21:00	Draco 2	C	30	X	X	X	X				X
15 October 2023	18:45-20:00	Draco 2	C	63	X	X	X	X	X	X	X	X
16 October 2023	19:00-20:15	East-16	C	40	X		X	X	X	X	X	X
22 October 2023	19:00-20:00	Draco 2	C	48	X	X	X	X	X	X	X	X
1 November 2023	22:00-23:15	Draco 2	C	32		X	X	X				
5 November 2023	20:30-21:00	Draco 2	C	12		X						
6 November 2023	21:00-21:45	East-16, West-14	C	32		X			X	X	X	X
7 November 2023	20:30-21:00	Draco2, East-16	C	27		X	X		X	X	X	X
10 November 2023	21:00-22:30	pt5m	V	40	X	X	X				X	X
12 November 2023	21:00-23:00	pt5m	V	40		X	X		X	X	X	X

TABLE IX: Record of the dates and times observation were taken for each target

B. Data Obtained by 2002 NW16

Date	Time (UTC)	Telescope	RA (hh:mm:ss.ss)	JPL RA (hh:mm:ss.s)	dRA (s.s)	Dec (dd:mm:ss.s)	JPL Dec (dd:mm:ss.s)	dDec (s.s)	Total Uncertainty (s.s)	V-Band m
25 September 2023	21:12:15	Draco 2	21:15:01.52	21:15:03.17	-1.65	+63:44:18.4	+63:44:18.6	-0.2	0.30	17.5
01 October 2023	21:21:07	Draco 2	21:03:04.48	21:03:05.24	-0.76	+62:54:20.1	+62:54:20.8	-0.7	0.25	17.6
14 October 2023	20:36:09	Draco 2	20:55:48.41	20:55:48.09	0.32	+60:11:44.3	+60:11:45.2	-0.9	0.25	17.8
15 October 2023	19:17:26	Draco 2	20:56:10.85	20:56:10.05	0.80	+59:58:06.6	+59:58:07.1	-0.5	0.29	17.8
16 October 2023	19:50:48	East-16	20:56:41.21	20:56:41.26	-0.05	+59:43:09.9	+59:43:10.5	-0.6	0.23	17.8
22 October 2023	19:34:00	Draco 2	21:02:05.25	21:02:04.99	0.26	+58:12:55.0	+58:12:55.4	-0.4	0.27	17.8
01 October 2023	22:34:25	Draco 2	21:19:09.74	21:19:11.40	-1.66	+55:32:36.5	+55:32:37.0	0.5	0.31	17.9
07 October 2023	21:12:26	Draco2	21:33:05.58	21:33:04.72	0.86	+53:54:04.2	+53:54:04.6	-0.4	0.33	17.9
10 October 2023	21:13:37	pt5m	21:41:04.86	21:41:03.70	1.16	+53:03:06.3	+53:03:07.3	-1.0	0.15	17.9
12 October 2023	22:44:51	pt5m	21:46:54.30	21:46:52.64	1.66	+52:27:17.4	+52:27:18.1	0.7	0.14	17.9

TABLE X: Record of the dates and times observation were taken for each target

C. Error in Celestial Coordinates

3. 2001 XR31

1. 2008 QY

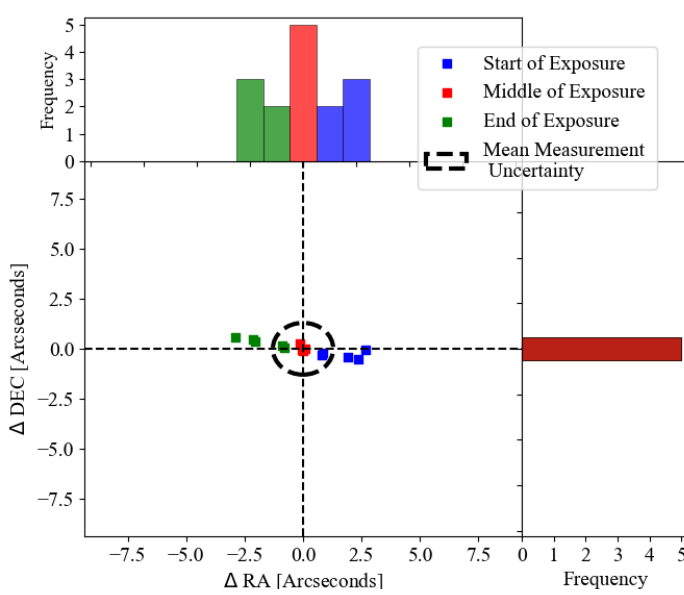


FIG. 12: The deviation of all our calculated celestial coordinates, RA and DEC, from JPL horizons' predictions for 2008 QY. The deviations are calculated using three comparative JPL data points at the start, middle and end of each observation, to show potential errors created from incorrect time stamps during orbital fitting. Histograms are created using 15 bins across each dimension to show the data points' distribution and help identify systematic errors.

2. 1999 SL5

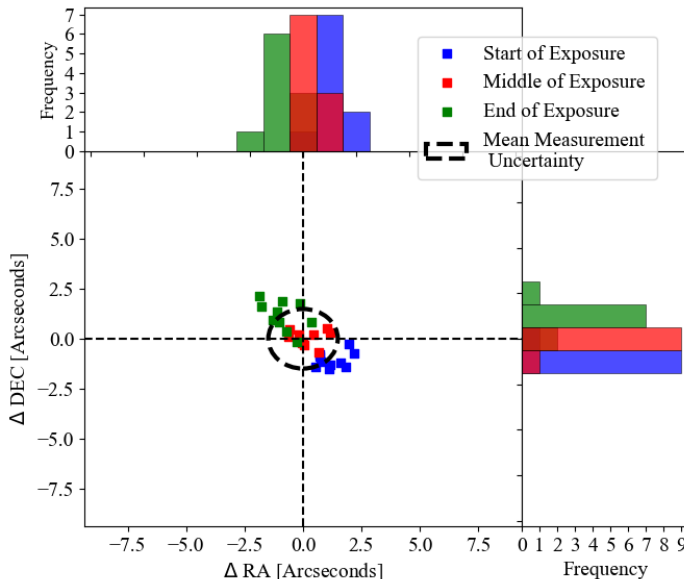


FIG. 13: The deviation of all our calculated celestial coordinates, RA and DEC, from JPL horizons' predictions for 1999 SL5. The deviations are calculated using three comparative JPL data points at the start, middle and end of each observation, to show potential errors created from incorrect time stamps during orbital fitting. Histograms are created using 15 bins across each dimension to show the data points' distribution and help identify systematic errors.

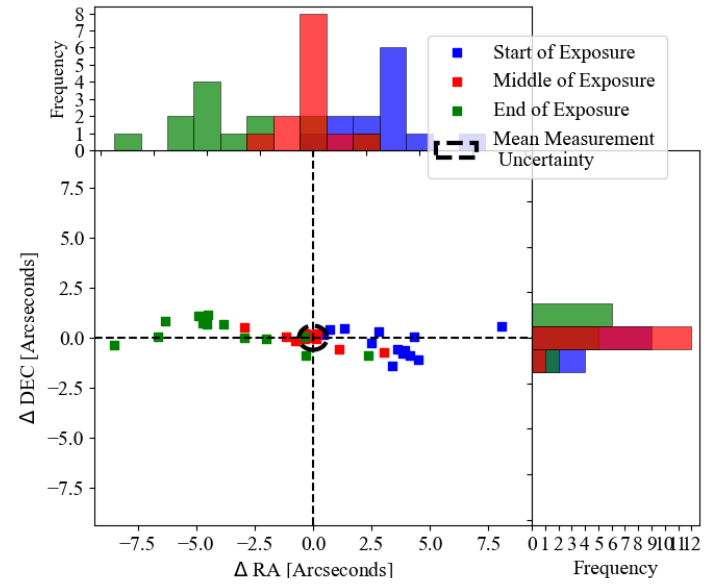


FIG. 14: The deviation of all our calculated celestial coordinates, RA and DEC, from JPL horizons' predictions for 2001 XR31. The deviations are calculated using three comparative JPL data points at the start, middle and end of each observation, to show potential errors created from incorrect time stamps during orbital fitting. Histograms are created using 15 bins across each dimension to show the data points' distribution and help identify systematic errors.

4. A872 GB

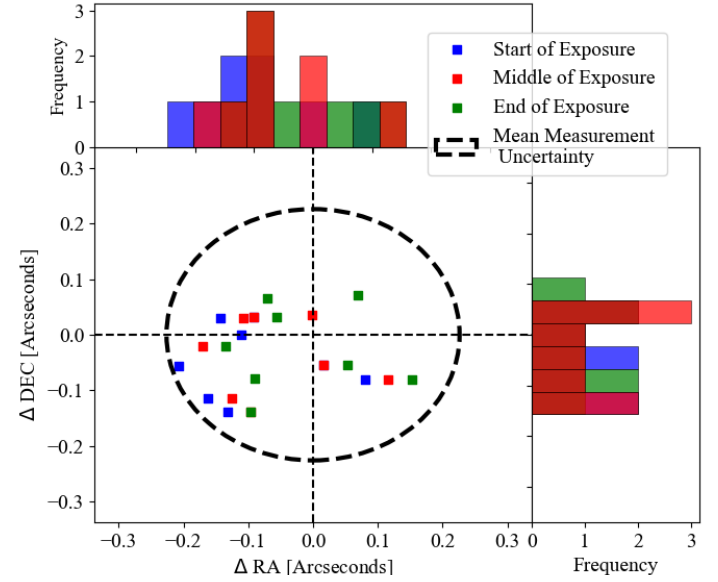


FIG. 15: The deviation of all our calculated celestial coordinates, RA and DEC, from JPL horizons' predictions for A872 GB. The deviations are calculated using three comparative JPL data points at the start, middle and end of each observation, to show potential errors created from incorrect time stamps during orbital fitting. Histograms are created using 15 bins across each dimension to show the data points' distribution and help identify systematic errors.

5. A866 LA

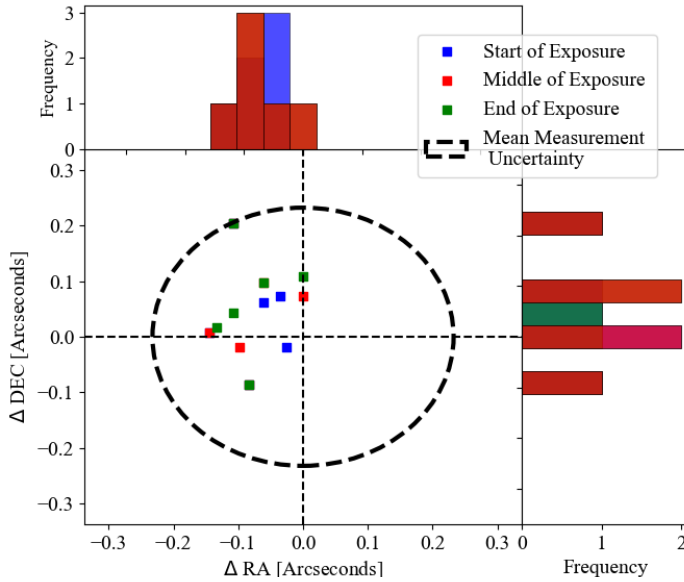


FIG. 16: The deviation of all our calculated celestial coordinates, RA and DEC, from JPL horizons' predictions for A866 LA. The deviations are calculated using three comparative JPL data points at the start, middle and end of each observation, to show potential errors created from incorrect time stamps during orbital fitting. Histograms are created using 15 bins across each dimension to show the data points' distribution and help identify systematic errors.

7. A854 EB

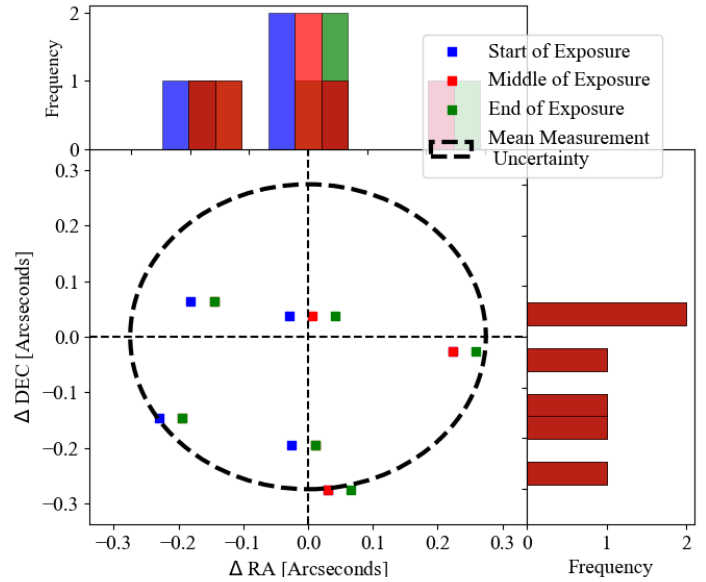


FIG. 18: The deviation of all our calculated celestial coordinates, RA and DEC, from JPL horizons' predictions for A854 EB. The deviations are calculated using three comparative JPL data points at the start, middle and end of each observation, to show potential errors created from incorrect time stamps during orbital fitting. Histograms are created using 15 bins across each dimension to show the data points' distribution and help identify systematic errors.

6. A852 VA

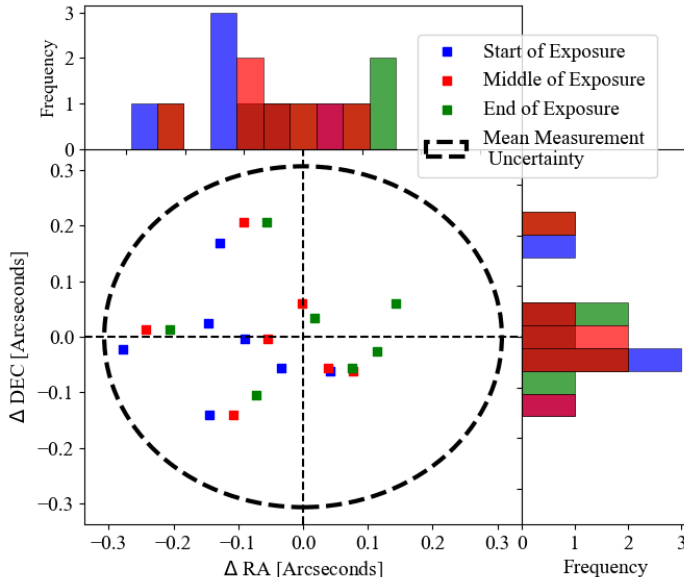


FIG. 17: The deviation of all our calculated celestial coordinates, RA and DEC, from JPL horizons' predictions for A852 VA. The deviations are calculated using three comparative JPL data points at the start, middle and end of each observation, to show potential errors created from incorrect time stamps during orbital fitting. Histograms are created using 15 bins across each dimension to show the data points' distribution and help identify systematic errors.

D. Cumulative Probability Distributions

1. 2008 QY

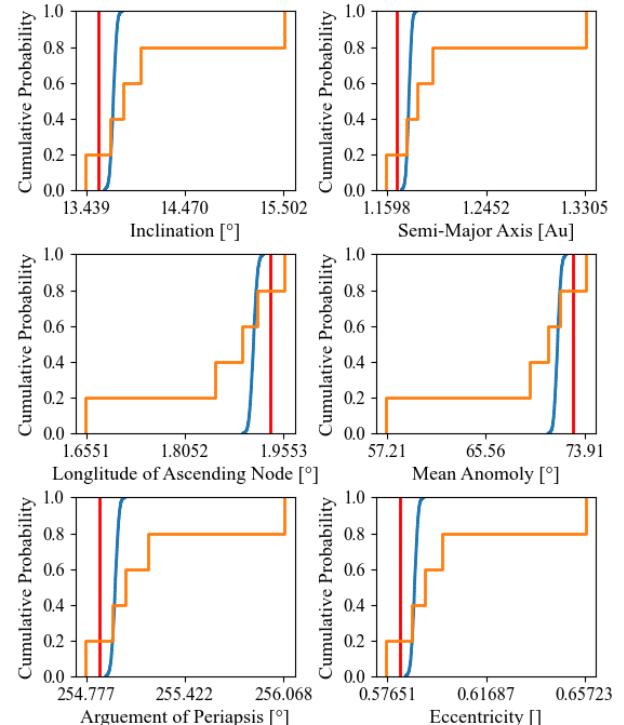


FIG. 19: The cumulative probability distributions of each element created through jackknife (orange) and observational Monte Carlo analysis (blue) for 2008 QY are plotted against one another for comparison. The accepted value of each element given by JPL Horizons (red) is also shown.

2. 1999 SL5

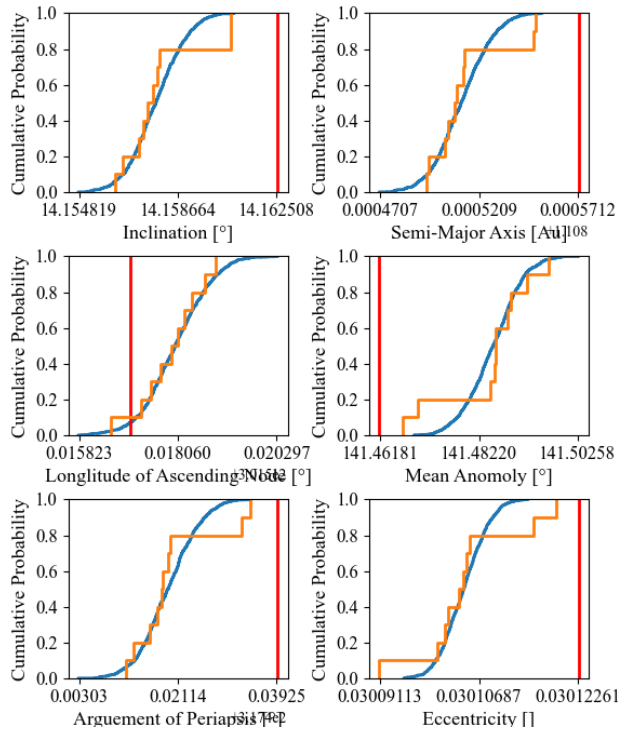


FIG. 20:

The cumulative probability distributions of each element created through jackknife (orange) and observational Monte Carlo analysis (blue) for 2002 NW16 are plotted against one another for comparison. The accepted value of each element given by JPL Horizons (red) is also shown.

4. A872 GB

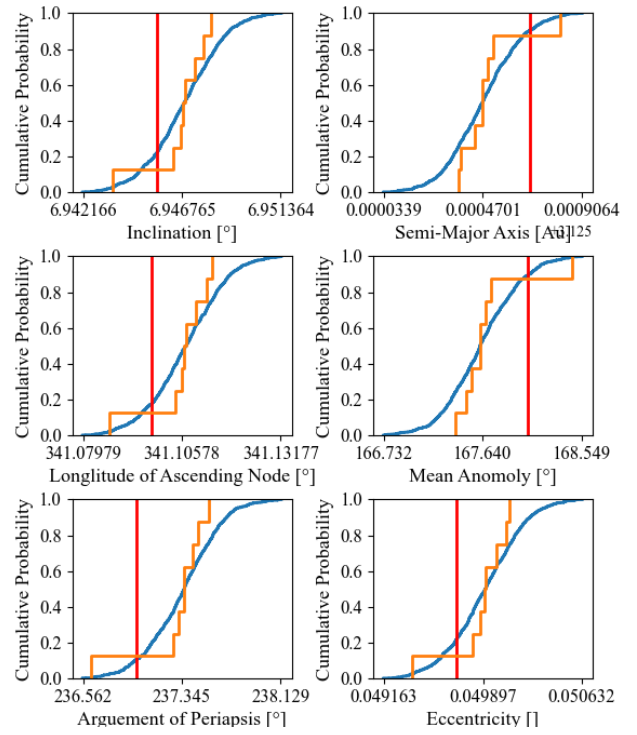


FIG. 22: The cumulative probability distributions of each element created through jackknife (orange) and observational Monte Carlo analysis (blue) for A872 GB are plotted against one another for comparison. The accepted value of each element given by JPL Horizons (red) is also shown.

3. 2001 XR31

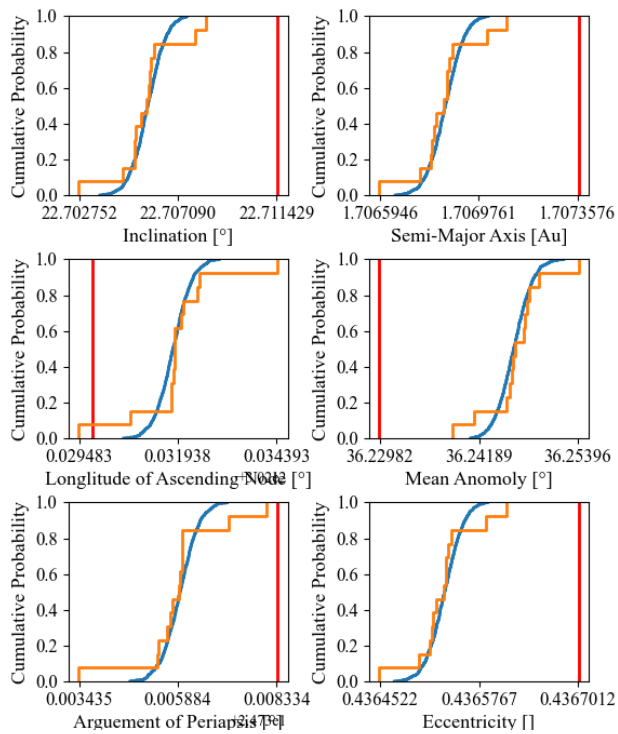


FIG. 21:

The cumulative probability distributions of each element created through jackknife (orange) and observational Monte Carlo analysis (blue) for 2001 XR31 are plotted against one another for comparison. The accepted value of each element given by JPL Horizons (red) is also shown.

5. A866 LA

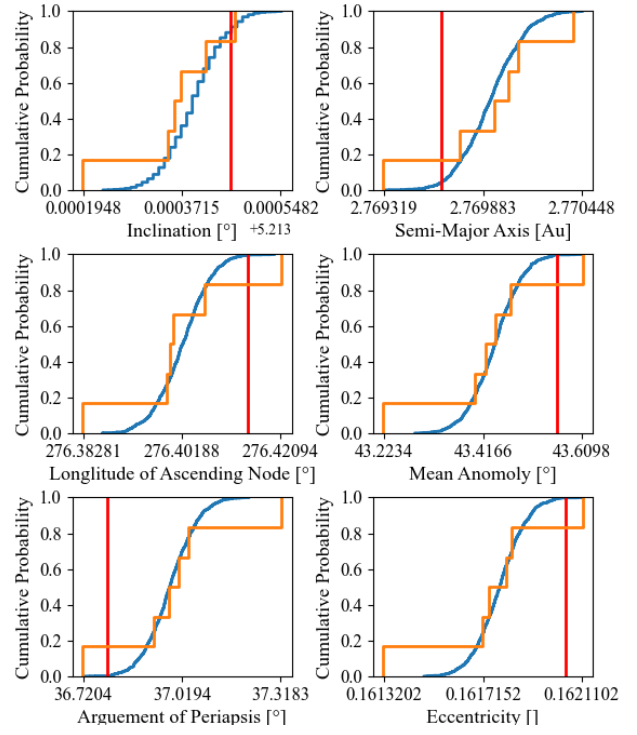


FIG. 23: The cumulative probability distributions of each element created through jackknife (orange) and observational Monte Carlo analysis (blue) for A866 LA are plotted against one another for comparison. The accepted value of each element given by JPL Horizons (red) is also shown.

6. A852 VA

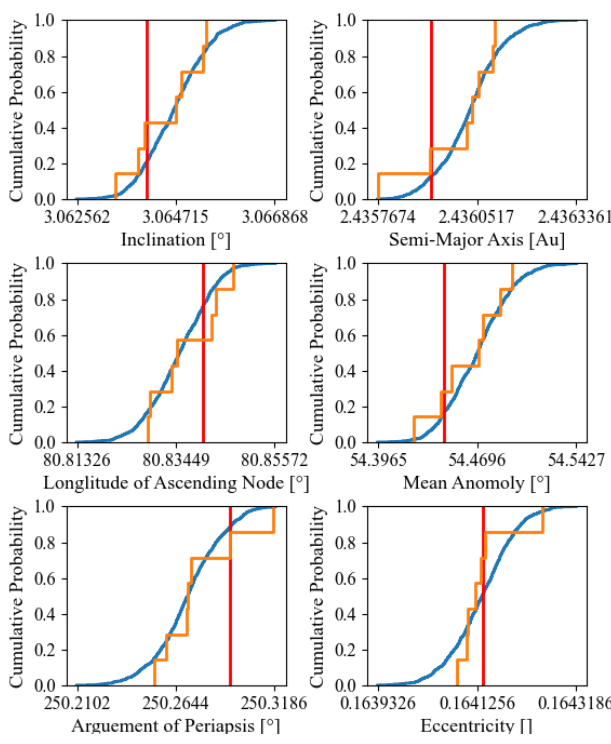


FIG. 24: The cumulative probability distributions of each element created through jackknife (orange) and observational Monte Carlo analysis (blue) for A852 VA are plotted against one another for comparison. The accepted value of each element given by JPL Horizons (red) is also shown.

7. A854 EB

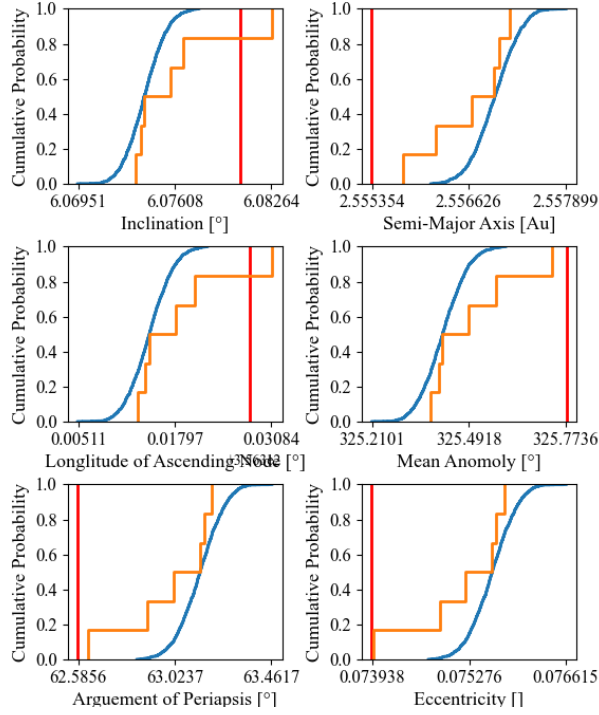


FIG. 25: The cumulative probability distributions of each element created through jackknife (orange) and observational Monte Carlo analysis (blue) for A854 EB are plotted against one another for comparison. The accepted value of each element given by JPL Horizons (red) is also shown.

E. Comparison of Observational Monte Carlo and Jackknife Uncertainties

1. 2008 QY

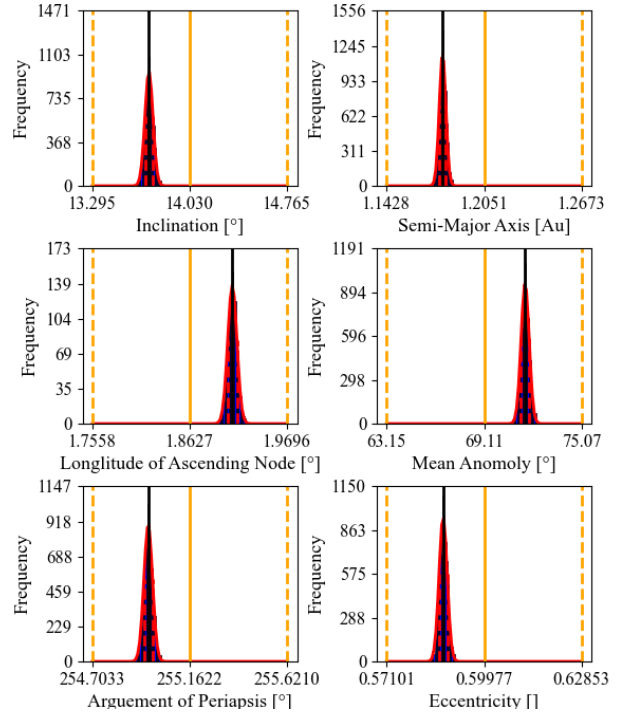


FIG. 26: 2008 QY's determined orbital elements from Find Orb using the full observational sample (black), the jackknife mean (orange solid), and the mean from the Gaussian distribution (red solid) fitted to observational Monte Carlo's results (blue) are plotted against each other. The one-sigma error given by Monte Carlo (red dashed) and jackknifing (orange dashed) are also marked.

2. 1999 SLS

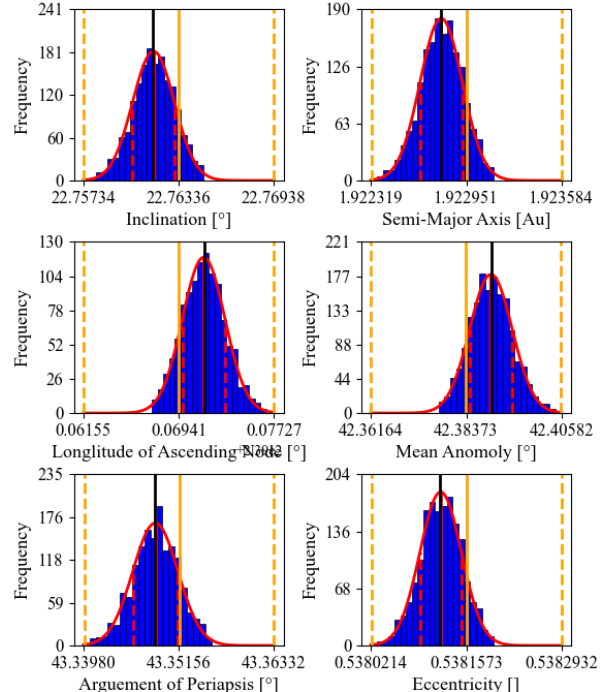


FIG. 27: 1999 SLS's determined orbital elements from Find Orb using the full observational sample (black), the jackknife mean (orange solid), and the mean from the Gaussian distribution (red solid) fitted to observational Monte Carlo's results (blue) are plotted against each other. The one-sigma error given by Monte Carlo (red dashed) and jackknifing (orange dashed) are also marked.

3. 2001 XR31

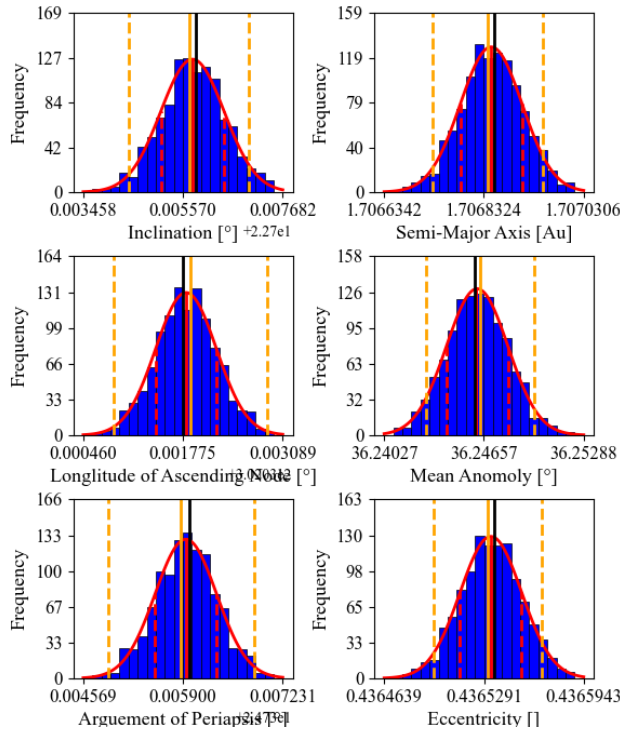


FIG. 28: 2001 XR31's determined orbital elements from Find Orb using the full observational sample (black), the jackknife mean (orange solid), and the mean from the Gaussian distribution (red solid) fitted to observational Monte Carlo's results (blue) are plotted against each other. The one-sigma error given by Monte Carlo (red dashed) and jackknifing (orange dashed) are also marked.

5. A866 LA

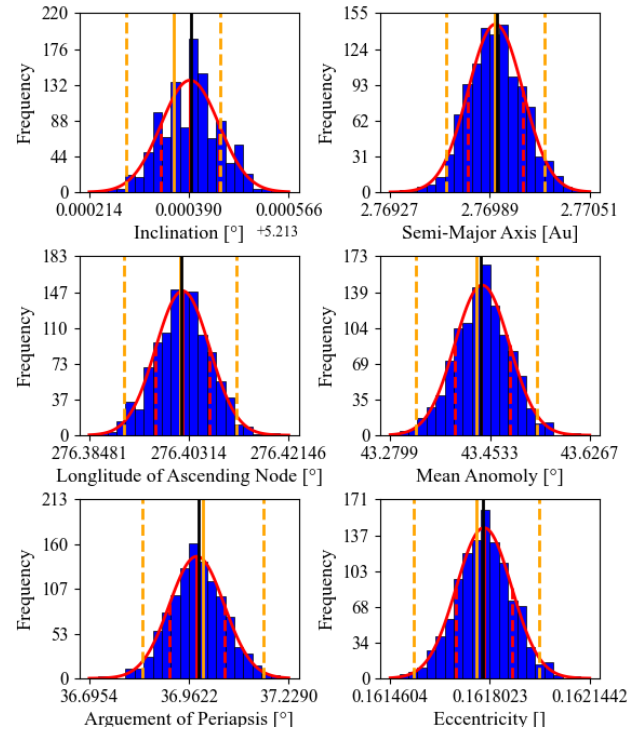


FIG. 30: A866 LA's determined orbital elements from Find Orb using the full observational sample (black), the jackknife mean (orange solid), and the mean from the Gaussian distribution (red solid) fitted to observational Monte Carlo's results (blue) are plotted against each other. The one-sigma error given by Monte Carlo (red dashed) and jackknifing (orange dashed) are also marked.

4. A872 GB

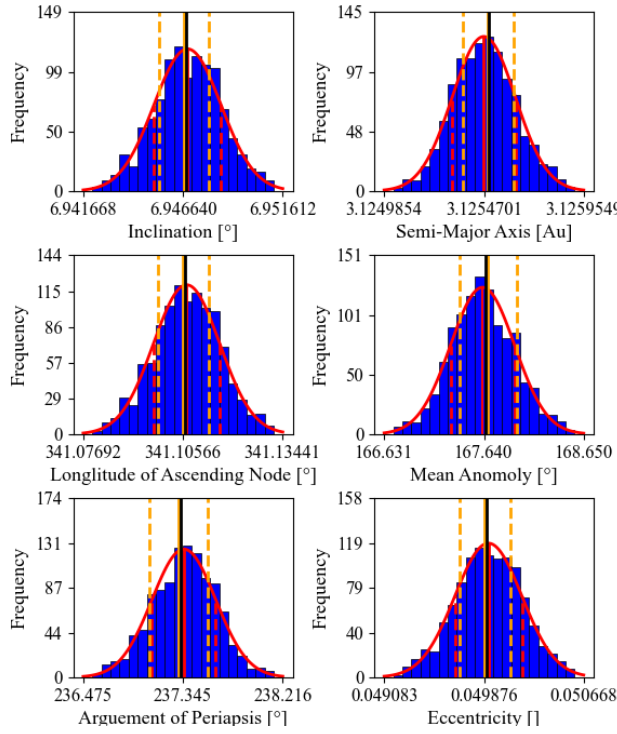


FIG. 29: A872 GB's determined orbital elements from Find Orb using the full observational sample (black), the jackknife mean (orange solid), and the mean from the Gaussian distribution (red solid) fitted to observational Monte Carlo's results (blue) are plotted against each other. The one-sigma error given by Monte Carlo (red dashed) and jackknifing (orange dashed) are also marked.

6. A852 VA

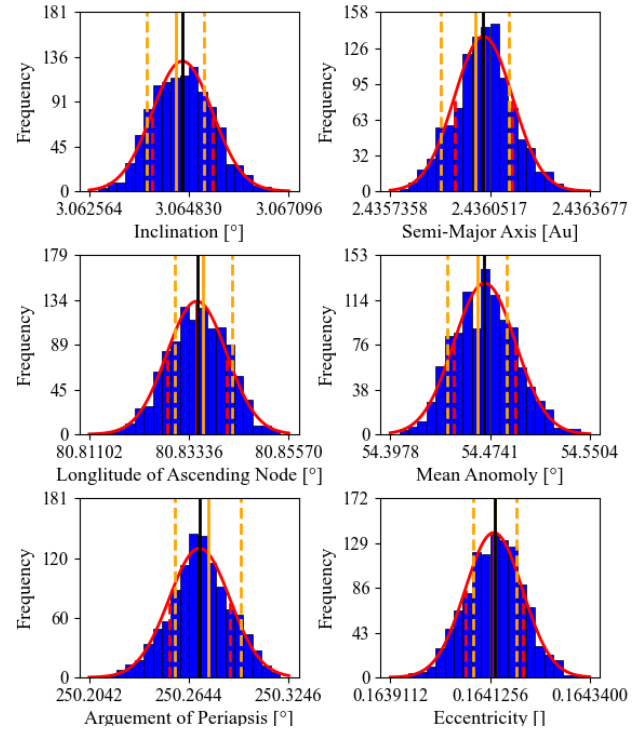


FIG. 31: A852 VA's determined orbital elements from Find Orb using the full observational sample (black), the jackknife mean (orange solid), and the mean from the Gaussian distribution (red solid) fitted to observational Monte Carlo's results (blue) are plotted against each other. The one-sigma error given by Monte Carlo (red dashed) and jackknifing (orange dashed) are also marked.

7. A854 EB

2. 1999 SL5

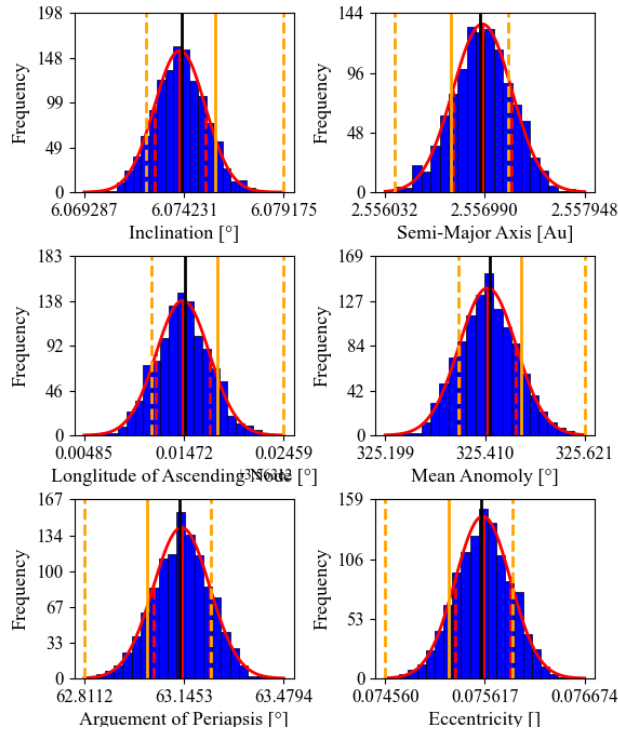


FIG. 32: A854 EB's determined orbital elements from Find Orb using the full observational sample (black), the jackknife mean (orange solid), and the mean from the Gaussian distribution (red solid) fitted to observational Monte Carlo's results (blue) are plotted against each other. The one-sigma error given by Monte Carlo (red dashed) and jackknifing (orange dashed) are also marked.

F. Orbital Elements

1. 2008 QY

Elements	Find Orb	JPL Horizons	Absolute Difference	Difference (one-Sigma errors)
<i>Eccentricity</i> []	0.588 ±0.001	0.582	0.006	5.11
<i>Semi Major Axis</i> [Au]	1.179 ±0.002	1.168	0.011	5.01
<i>Inclination</i> [°]	13.72 ±0.03	13.57	0.16	5.12
<i>Argument of Periapsis</i> [°]	254.97 ±0.02	254.86	0.10	5.04
<i>Longitude of the ascending node</i> [°]	1.909 ±0.005	1.934	0.025	4.94
<i>Mean Anomaly</i> [°]	71.6 ±0.2	72.9	1.3	5.12

TABLE XI: Orbital elements for 2008 QY

Elements	Find Orb	JPL Horizons	Absolute Difference	Difference (one-Sigma errors)
<i>Eccentricity</i> []	0.53812 ±0.00003	0.53826	0.00015	4.96
<i>Semi Major Axis</i> [Au]	1.9228 ±0.0001	1.9235	0.0007	4.81
<i>Inclination</i> [°]	22.762 ±0.001	22.768	0.006	4.91
<i>Argument of Periapsis</i> [°]	43.346 ±0.003	43.360	0.012	4.22
<i>Longitude of the ascending node</i> [°]	239.072 ±0.001	239.064	0.008	4.52
<i>Mean Anomaly</i> [°]	42.390 ±0.005	42.366	0.023	4.76

TABLE XII: Orbital elements for 1999 SL5

3. 2001 XR31

Elements	Find Orb	JPL Horizons	Absolute Difference	Difference (one-Sigma errors)
<i>Eccentricity</i> []	0.43654 ±0.00002	0.43670	0.00017	8.29
<i>Semi Major Axis</i> [Au]	1.70685 ±0.00006	1.70736	0.00051	8.28
<i>Inclination</i> [°]	22.7058 ±0.0007	22.7115	0.0056	8.39
<i>Argument of Periapsis</i> [°]	24.7360 ±0.0004	24.7384	0.0024	5.78
<i>Longitude of the ascending node</i> [°]	302.0318 ±0.0004	302.0298	0.0020	4.90
<i>Mean Anomaly</i> [°]	36.246 ±0.002	36.230	0.016	8.35

TABLE XIII: Orbital elements for 2001 XR31

4. A872 GB

Elements	Find Orb	JPL Horizons	Absolute Difference	Difference (one-Sigma errors)
<i>Eccentricity</i> []	0.0499 ±0.0003	0.0497	0.0002	0.72
<i>Semi Major Axis</i> [Au]	3.1255 ±0.0002	3.1257	0.0002	1.19
<i>Inclination</i> [°]	6.947 ±0.002	6.946	0.001	0.71
<i>Argument of Periapsis</i> [°]	237.3 ±0.3	237.0	0.3	1.22
<i>Longitude of the ascending node</i> [°]	341.11 ±0.01	341.10	0.01	0.87
<i>Mean Anomaly</i> [°]	167.7 ±0.3	168.1	0.4	1.22

TABLE XIV: Orbital elements for A872 GB

5. A852 VA

H. Geocentric Distance Over Time

I. 2002 NW16

Elements	Find Orb	JPL Horizons	Absolute Difference	Difference (one-Sigma errors)
Eccentricity [η]	0.16414 ± 0.00006	0.16414	0.00000	0.03
Semi Major Axis [Au]	2.43603 ± 0.00009	2.43592	0.00011	1.22
Inclination [$^\circ$]	3.0647 ± 0.0007	3.0641	0.0006	0.85
Argument of Periapsis [$^\circ$]	250.27 ± 0.02	250.29	0.02	1.26
Longitude of the ascending node [$^\circ$]	80.835 ± 0.007	80.840	0.005	0.75
Mean Anomaly [$^\circ$]	54.47 ± 0.02	54.45	0.02	1.03

TABLE XV: Orbital elements for A852 VA

6. A854 EB

Elements	Find Orb	JPL Horizons	Absolute Difference	Difference (one-Sigma errors)
Eccentricity [η]	0.0756 ± 0.0003	0.0739	0.0016	5.6204
Semi Major Axis [Au]	2.5569 ± 0.0003	2.5553	0.0016	5.6667
Inclination [$^\circ$]	6.074 ± 0.001	6.080	0.006	5.058
Argument of Periapsis [$^\circ$]	63.13 ± 0.09	62.58	0.55	5.80
Longitude of the ascending node [$^\circ$]	356.315 ± 0.003	356.328	0.013	4.946
Mean Anomaly [$^\circ$]	325.42 ± 0.06	325.78	0.36	5.89

TABLE XVI: Orbital elements for A854 EB

G. Orbits within Celestial Plane

I. Main Belt Asteroids

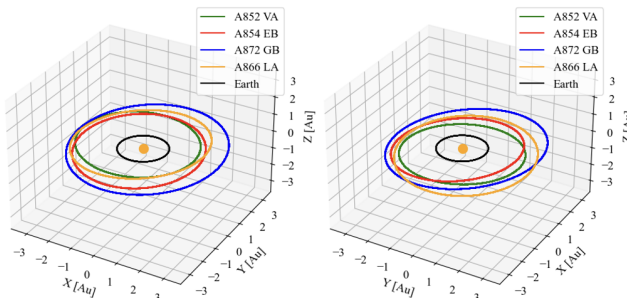


FIG. 33: A 3-D Cartesian representation of the heliocentric orbits of our target MB asteroids within the solar system ecliptic plane. The uncertainty in the orbits' trajectories calculated through orbital Monte Carlo is represented by their thickness. The Sun's fixed position at the origin and the Earth Orbit are also shown.

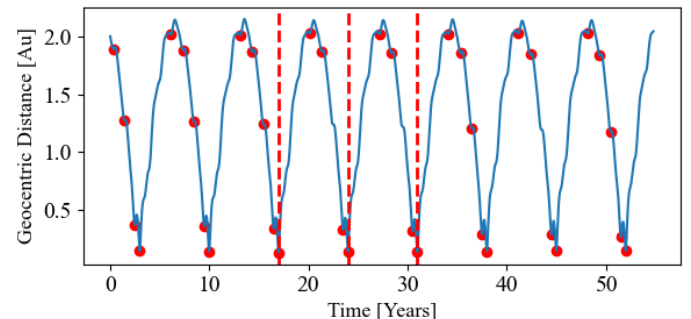


FIG. 34: The geocentric distance of 2002 NW16 over 20,000 days from the 12th November 2023 is shown (blue). All minimum turning points are marked (red dot) and the three closest approaches are highlighted (red dashed).

2. 1999 SL5

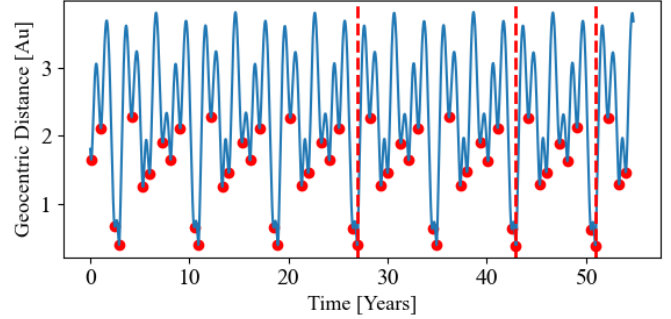


FIG. 35: The geocentric distance of 1999 SL5 over 20,000 days from the 12th November 2023 is shown (blue). All minimum turning points are marked (red dot) and the three closest approaches are highlighted (red dashed).

3. 2001 XR31

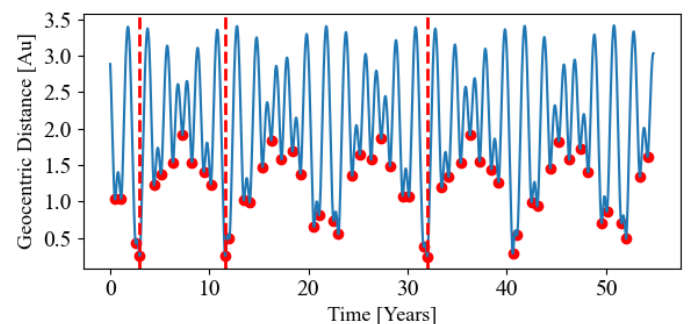


FIG. 36: The geocentric distance of 2001 XR31 over 20,000 days from the 12th November 2023 is shown (blue). All minimum turning points are marked (red dot) and the three closest approaches are highlighted (red dashed).

I. Close Approaches

1. 2002 NW16

Date	X [Au]	Y [Au]	Z [Au]	Total Distance [Au]
29 th October 2040	0.1017 ±0.0001	0.0722 ±0.0002	0.04656 ±0.00003	0.13314 ±0.00009
28 th October 2054	0.1224 ±0.0001	0.0410 ±0.0002	0.05358 ±0.00003	0.13314 ±0.00008
29 th October 2046	0.1188 ±0.0001	0.0608 ±0.0002	0.05173 ±0.00003	0.14313 ±0.00009

TABLE XVII: 2002 NW16's top three closest approaches

2. 1999 SL5

Date	X [Au]	Y [Au]	Z [Au]	Total Distance [Au]
8 th October 2074	0.2127 ±0.0002	-0.1059 ±0.0005	0.3064 ±0.0002	0.3877 ±0.0001
8 th October 2066	0.2116 ±0.0002	-0.1171 ±0.0005	0.3050 ±0.0002	0.3877 ±0.0002
8 th October 2050	0.2076 ±0.0002	-0.1282 ±0.0005	0.3072 ±0.0002	0.3877 ±0.0002

TABLE XVIII: 1999 SL5's top three closest approaches

3. 2001 XR31

Date	X [Au]	Y [Au]	Z [Au]	Total Distance [Au]
29 th October 2055	0.11292 ±0.00006	0.00115 ±0.00006	0.21780 ±0.00003	0.24534 ±0.00003
30 th October 2026	0.13487 ±0.00006	-0.05371 ±0.00006	0.20684 ±0.00003	0.25271 ±0.00003
13 th June 2035	0.1076 ±0.0002	-0.18452 ±0.00003	0.13776 ±0.00005	0.25417 ±0.00005

TABLE XIX: 2001 XR31's top three closest approaches

J. Spread of Virtual Asteroids and Positional Uncertainty Derivations

1. 2002 NW16 - 29th October 2040

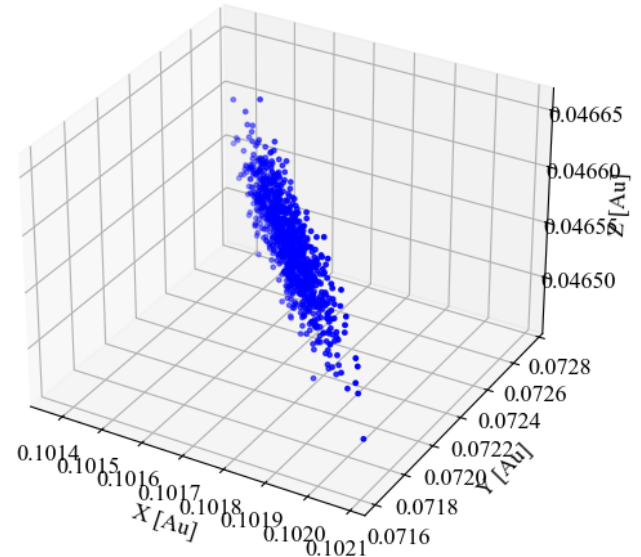


FIG. 37:

The geocentric positions of 1000 virtual asteroids of 2002 NW16 on 29th October 2040 are shown, calculated via orbital Monte Carlo from elements defined on the 12th of November 2023.

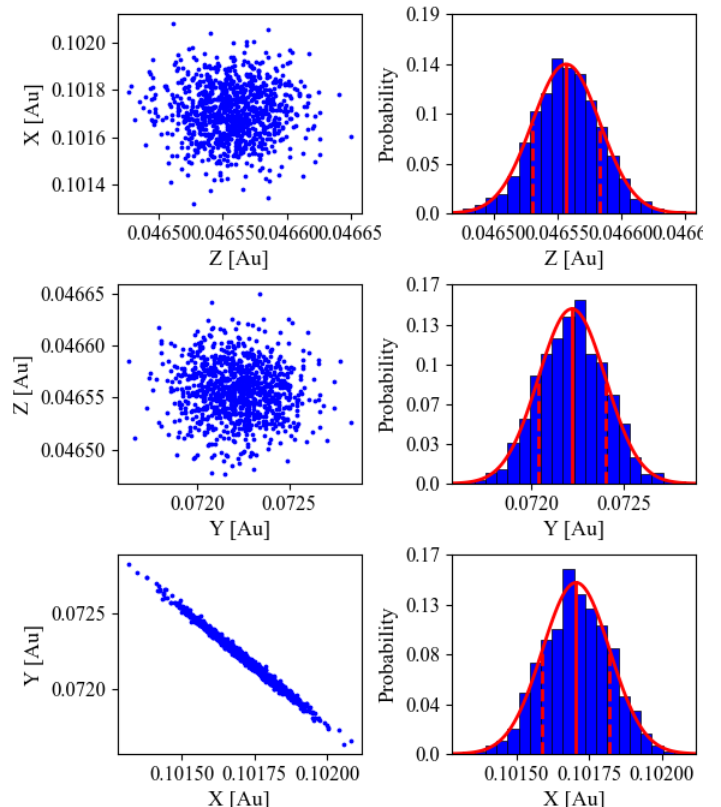
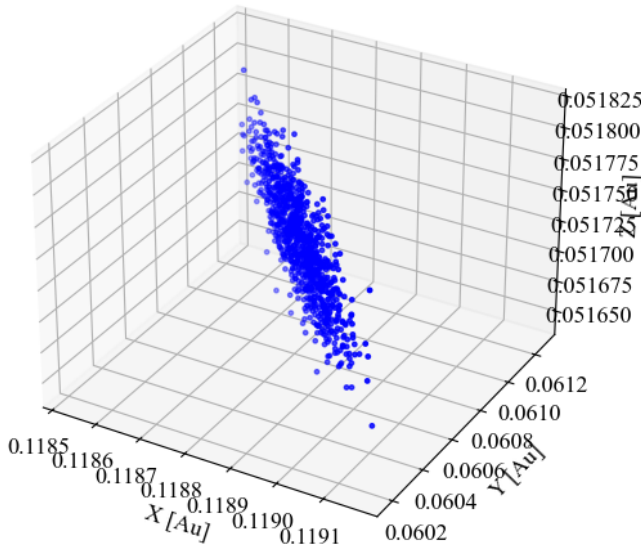


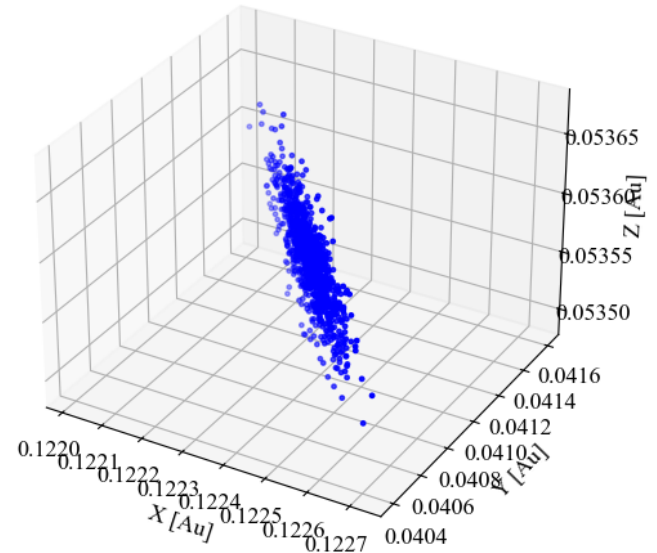
FIG. 38: The geocentric positions of 1000 virtual asteroids of 2002 NW16 on 29th October 2040 are plotted in 3 planes (XY, YZ, ZX). The distribution in each dimension is shown in the histogram, created from 20 bins, with the fitted Gaussian distribution shown and the corresponding mean (red solid) and one sigma error bars (red dashed).

2. 2002 NW16 - 29th October 2046

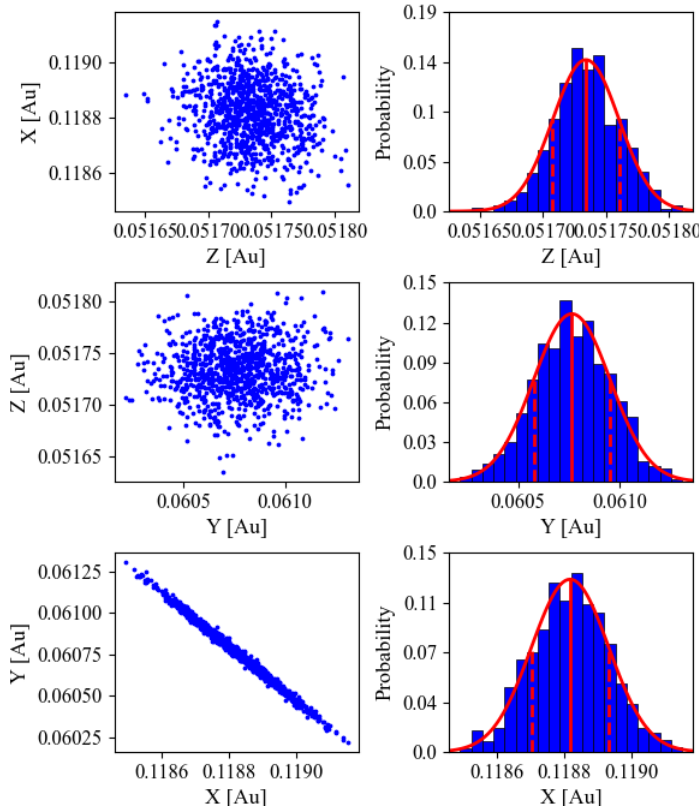
3. 2002 NW16 - 28th October 2054

**FIG. 39:**

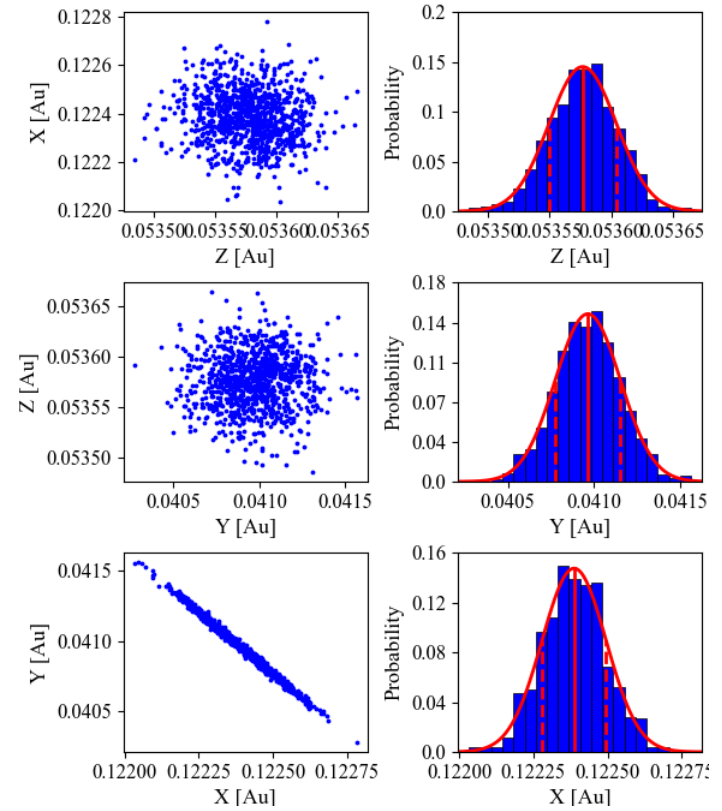
The geocentric positions of 1000 virtual asteroids of 2002 NW16 on 29th October 2046 are shown, calculated via orbital Monte Carlo from elements defined on the 12th of November 2023.

**FIG. 41:**

The geocentric positions of 1000 virtual asteroids of 2002 NW16 on 28th October 2054 are shown, calculated via orbital Monte Carlo from elements defined on the 12th of November 2023.

**FIG. 40:** The geocentric positions of 1000 virtual asteroids

of 2002 NW16 on 29th October 2046 are plot in 3 planes (XY, YZ, ZX).The distribution in each dimension is shown in the histogram, created from 20 bins, with the fitted Gaussian distribution shown and the corresponding mean (red solid) and one sigma error bars (red dashed)

**FIG. 42:** The geocentric positions of 1000 virtual asteroids

of 2002 NW16 on 28th October 2054 are plot in 3 planes (XY, YZ, ZX).The distribution in each dimension is shown in the histogram, created from 20 bins, with the fitted Gaussian distribution shown and the corresponding mean (red solid) and one sigma error bars (red dashed)

4. 2008 QY - 3rd October 2039

5. 2008 QY - 18th February 2054

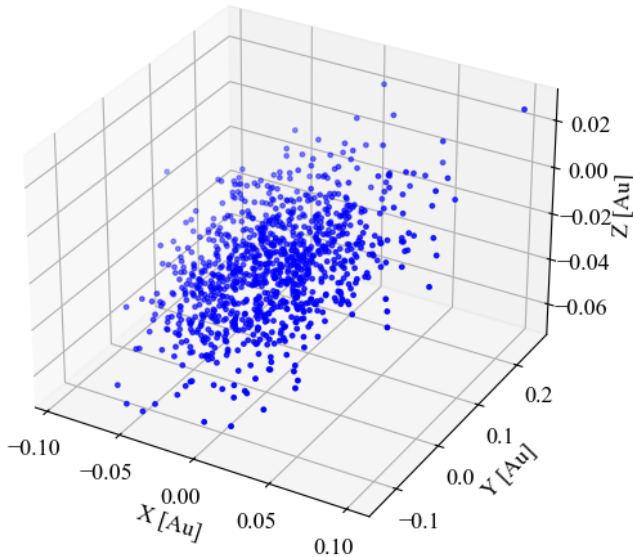


FIG. 43: The geocentric positions of 1000 virtual asteroids of 2008 QY on 3rd October 2039 are shown, calculated via orbital Monte Carlo from elements defined on the 12th of November 2023.

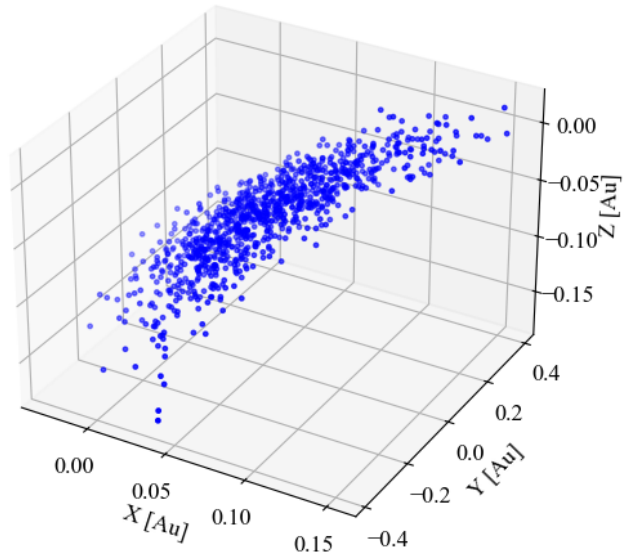


FIG. 45: The geocentric positions of 1000 virtual asteroids of 2008 QY on 18th February 2054 are shown, calculated via orbital Monte Carlo from elements defined on the 12th of November 2023.

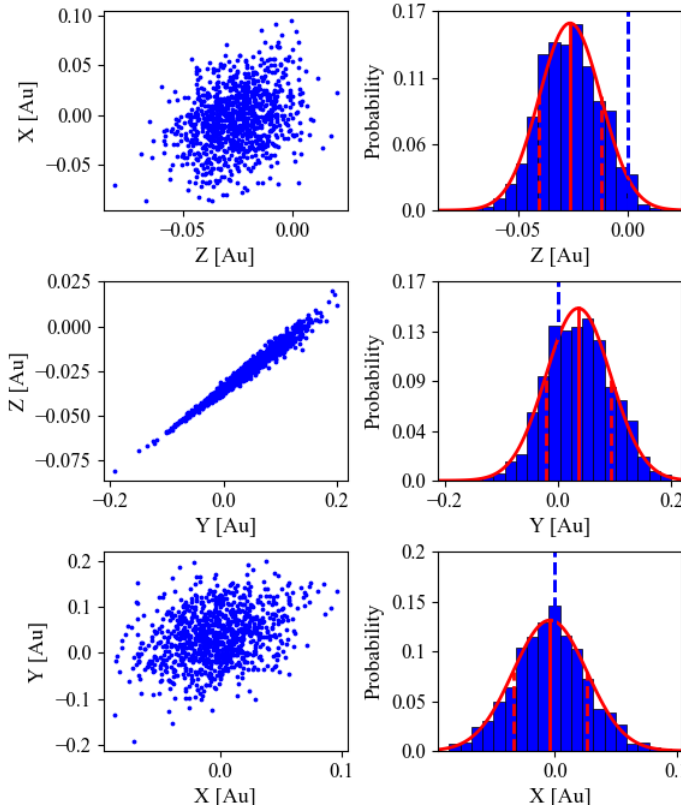


FIG. 44: The geocentric positions of 1000 virtual asteroids of 2008 QY on 3rd October 2039 are plot in 3 planes (XY, YZ, ZX). The distribution in each dimension is shown in the histogram, created from 20 bins, with the fitted Gaussian distribution shown and the corresponding mean (red solid) and one sigma error bars (red dashed)

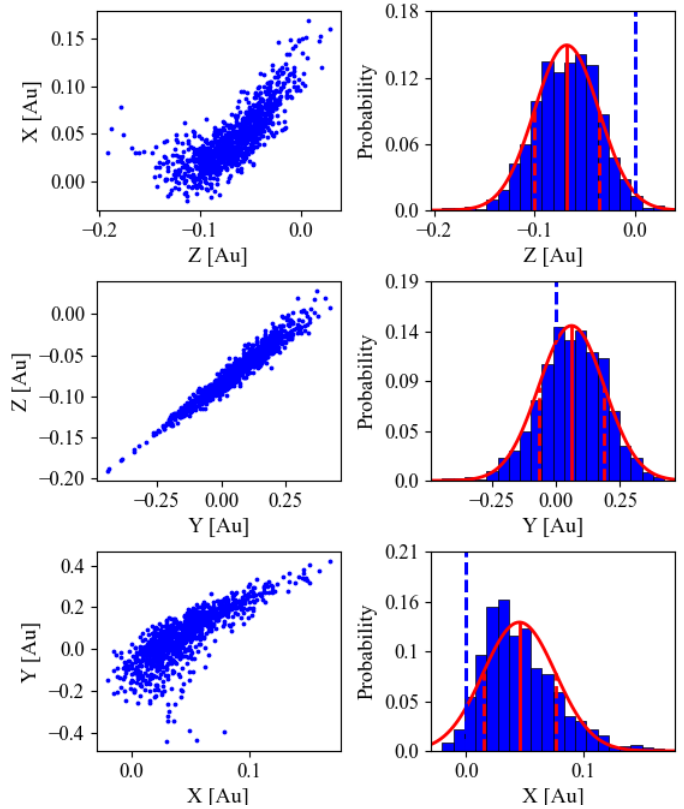
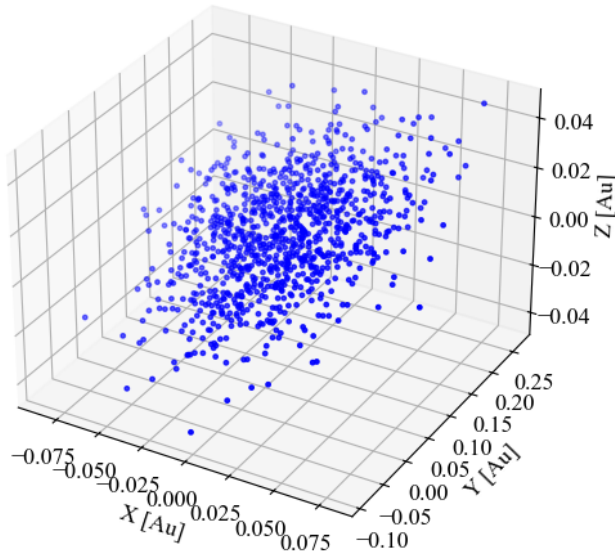


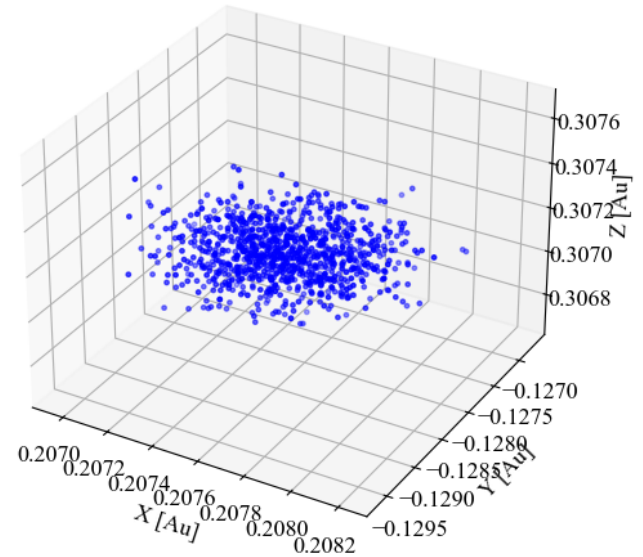
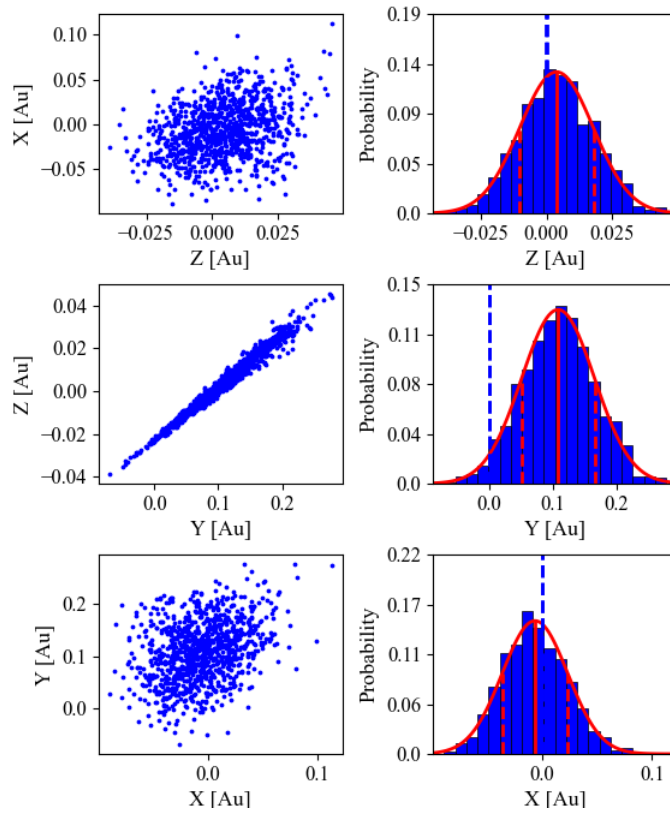
FIG. 46: The geocentric positions of 1000 virtual asteroids of 2008 QY on 18th February 2054 are plot in 3 planes (XY, YZ, ZX). The distribution in each dimension is shown in the histogram, created from 20 bins, with the fitted Gaussian distribution shown and the corresponding mean (red solid) and one sigma error bars (red dashed). Earth's position is also shown for reference (orange dashed)

6. 2008 QY - 29th September 2071

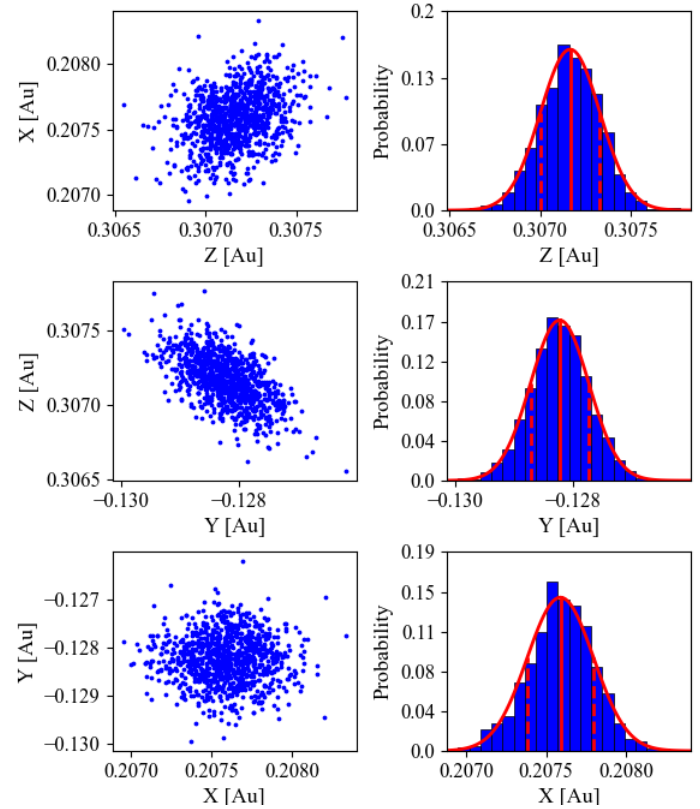
7. 1999 SL5 - 8th October 2050

**FIG. 47:**

The geocentric positions of 1000 virtual asteroids of 2008 QY on 29th September 2071 are shown, calculated via orbital Monte Carlo from elements defined on the 12th of November 2023.

**FIG. 49:** The geocentric positions of 1000 virtual asteroids of 1999 SL5 on 8th October 2050 are shown, calculated via orbital Monte Carlo from elements defined on the 12th of November 2023.**FIG. 48:**

The geocentric positions of 1000 virtual asteroids of 2008 QY on 29th September 2071 are plotted in 3 planes (XY, YZ, ZX). The distribution in each dimension is shown in the histogram, created from 20 bins, with the fitted Gaussian distribution shown and the corresponding mean (red solid) and one sigma error bars (red dashed). Earth's position is also shown for reference (orange dashed)

**FIG. 50:**

The geocentric positions of 1000 virtual asteroids of 1999 SL5 on 8th October 2050 are plotted in 3 planes (XY, YZ, ZX). The distribution in each dimension is shown in the histogram, created from 20 bins, with the fitted Gaussian distribution shown and the corresponding mean (red solid) and one sigma error bars (red dashed). Earth's position is also shown for reference (orange dashed)

8. 1999 SL5 - 8th October 2066

9. 1999 SL5 - 8th October 2074

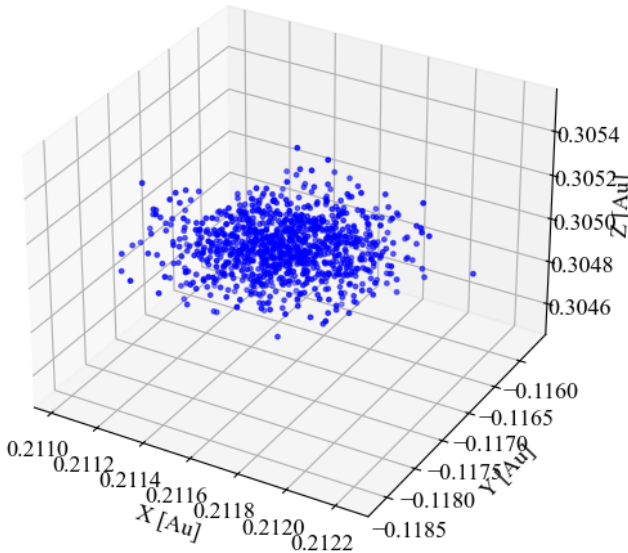


FIG. 51: The geocentric positions of 1000 virtual asteroids of 1999 SL5 on 8th October 2066 are shown, calculated via orbital Monte Carlo from elements defined on the 12th of November 2023.

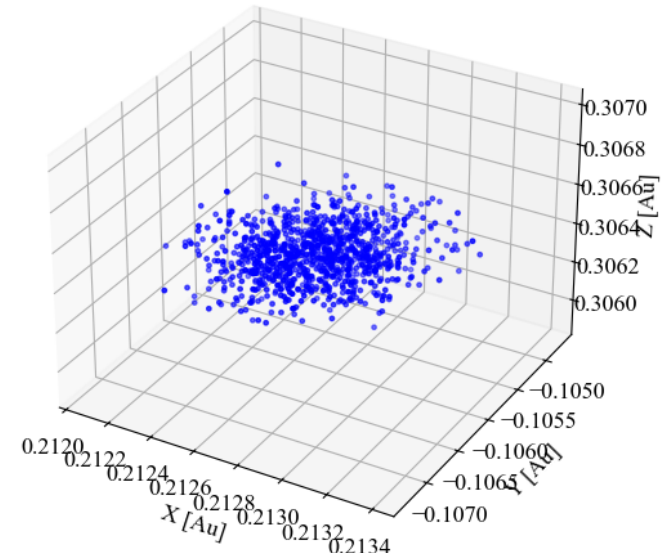


FIG. 53: The geocentric positions of 1000 virtual asteroids of 1999 SL5 on 8th October 2074 are shown, calculated via orbital Monte Carlo from elements defined on the 12th of November 2023.

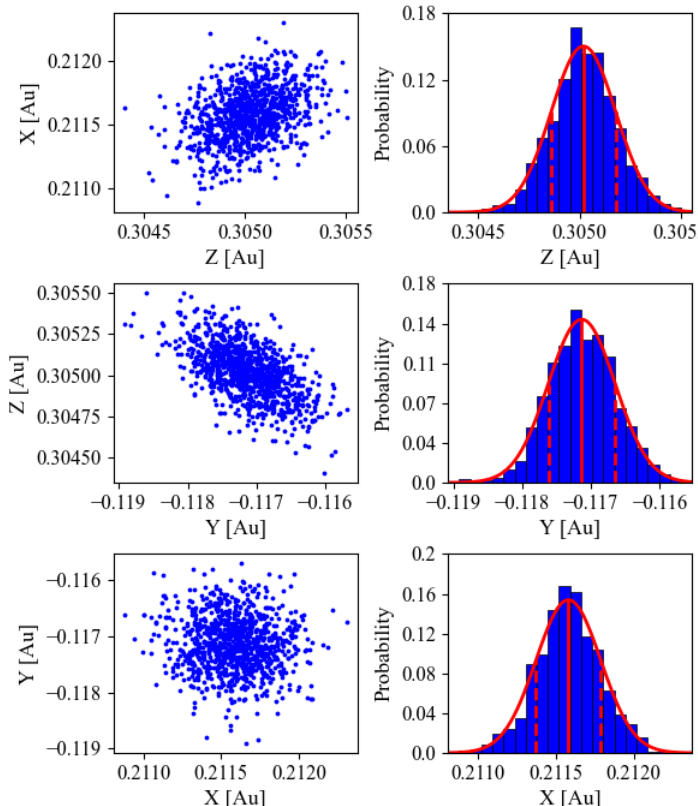


FIG. 52: The geocentric positions of 1000 virtual asteroids of 1999 SL5 on 8th October 2066 are plot in 3 planes (XY, YZ, ZX). The distribution in each dimension is shown in the histogram, created from 20 bins, with the fitted Gaussian distribution shown and the corresponding mean (red solid) and one sigma error bars (red dashed)

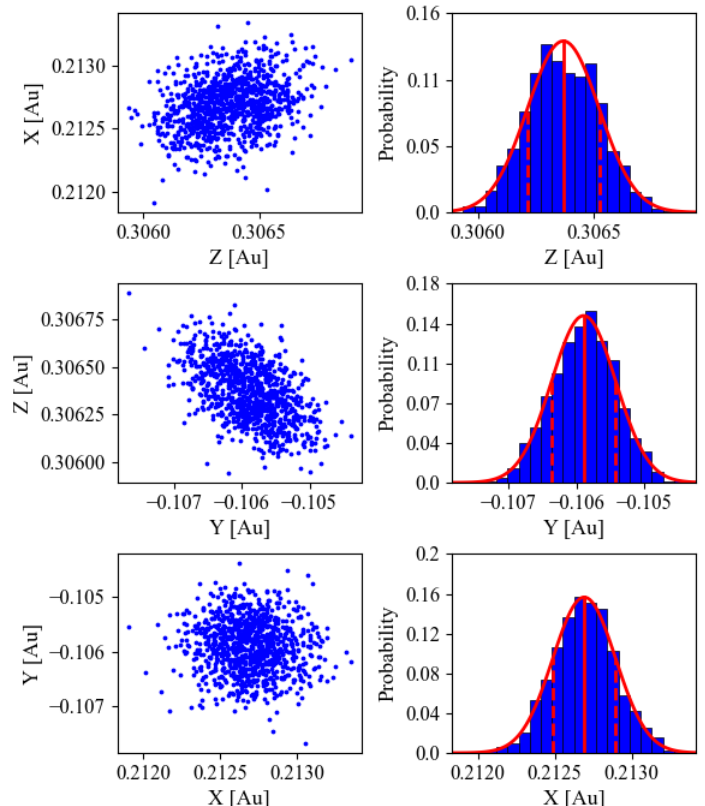
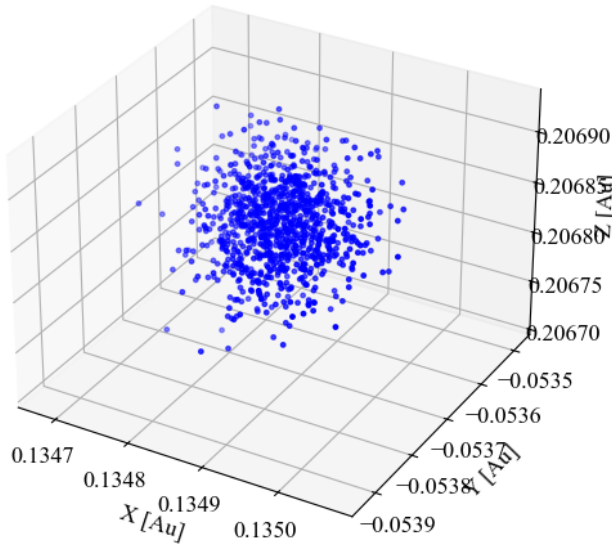


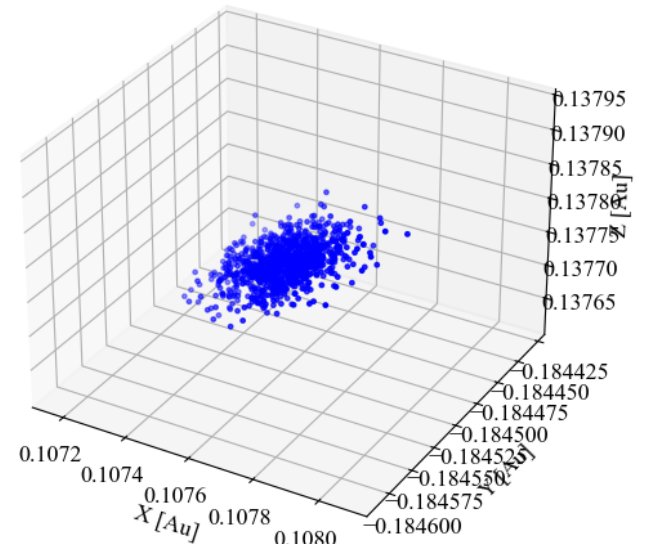
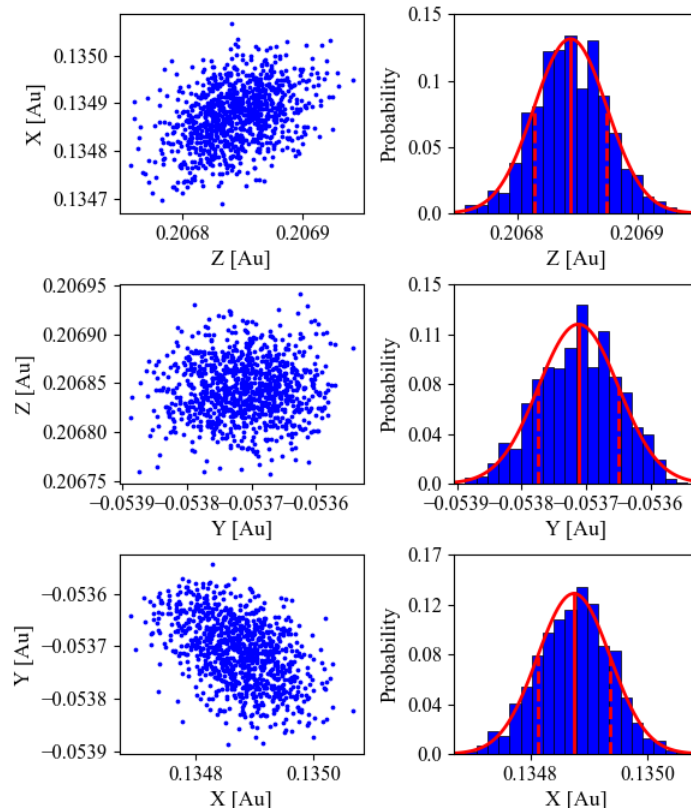
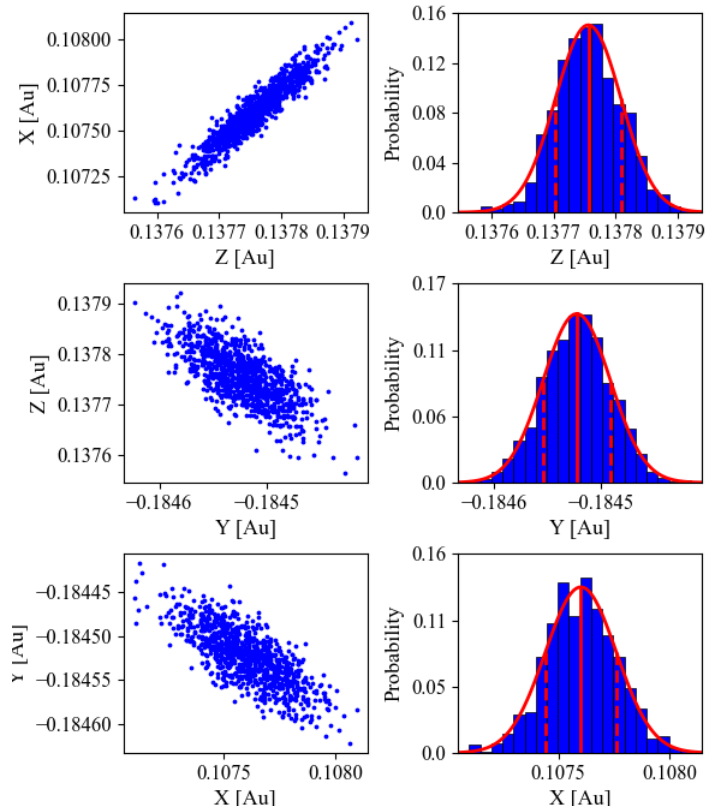
FIG. 54: The geocentric positions of 1000 virtual asteroids of 1999 SL5 on 8th October 2074 are plot in 3 planes (XY, YZ, ZX). The distribution in each dimension is shown in the histogram, created from 20 bins, with the fitted Gaussian distribution shown and the corresponding mean (red solid) and one sigma error bars (red dashed)

10. 2001 XR31- 30th October 2026

11. 2001 XR31 - 13th June 2035

**FIG. 55:**

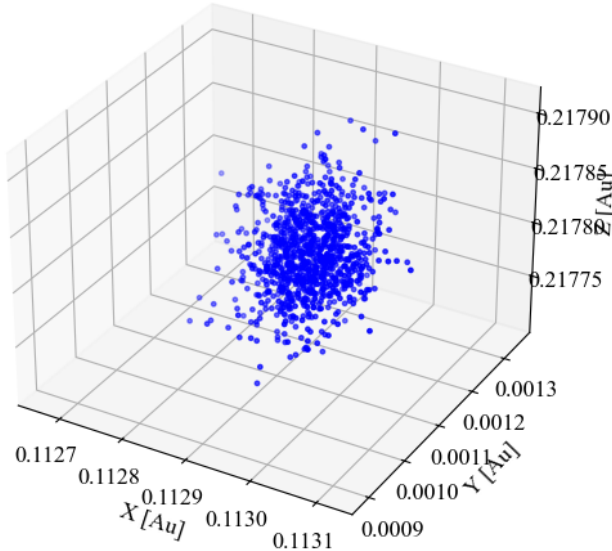
The geocentric positions of 1000 virtual asteroids of 2001 XR31 on 30th October 2026 are shown, calculated via orbital Monte Carlo from elements defined on the 12th of November 2023.

**FIG. 57:** The geocentric positions of 1000 virtual asteroids of 2001 XR31 on 13th June 2035 are shown, calculated via orbital Monte Carlo from elements defined on the 12th of November 2023.**FIG. 56:** The geocentric positions of 1000 virtual asteroids of 2001 XR31 on 30th October 2026 are plotted in 3 planes (XY, YZ, ZX). The distribution in each dimension is shown in the histogram, created from 20 bins, with the fitted Gaussian distribution shown and the corresponding mean (red solid) and one sigma error bars (red dashed)**FIG. 58:** The geocentric positions of 1000 virtual asteroids of 2001 XR31 on 13th June 2035 are plotted in 3 planes (XY, YZ, ZX). The distribution in each dimension is shown in the histogram, created from 20 bins, with the fitted Gaussian distribution shown and the corresponding mean (red solid) and one sigma error bars (red dashed)

12. 2001 XR31 - 29th October 2055

K. Fractional Change in Orbital Elements From Gravitational Perturbations

I. 2002 NW16

**FIG. 59:**

The geocentric positions of 1000 virtual asteroids of 2001 XR31 on 29th October 2055 are shown, calculated via orbital Monte Carlo from elements defined on the 12th of November 2023.

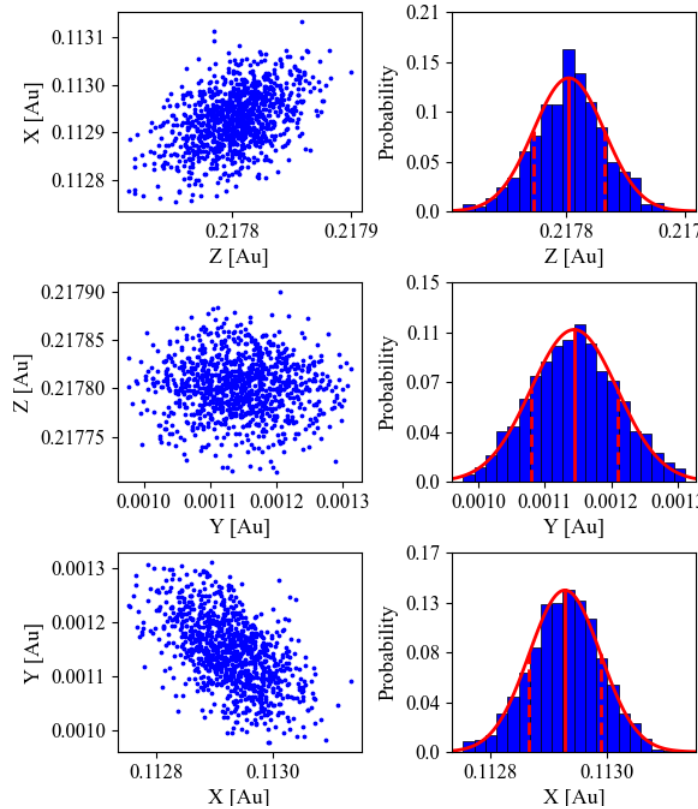
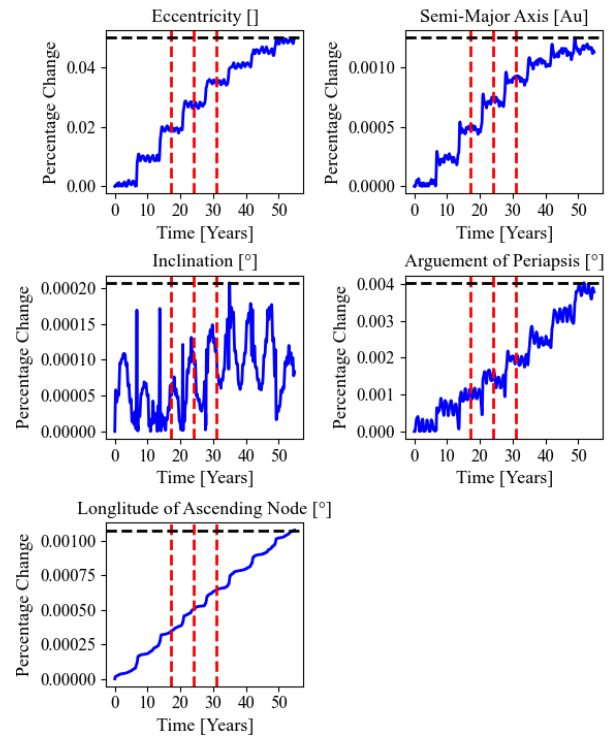


FIG. 60: The geocentric positions of 1000 virtual asteroids of 2001 XR31 on 29th October 2055 are plotted in 3 planes (XY, YZ, ZX). The distribution in each dimension is shown in the histogram, created from 20 bins, with the fitted Gaussian distribution shown and the corresponding mean (red solid) and one sigma error bars (red dashed)

**FIG. 61:** The fractional change (orange) in the orbital elements

of 2002 NW16 defined on the 12th November 2023 over 20,000 days with days of closest approaches to Earth marked (dashed red) and the maximum fractional change (dashed black)

2. 2008 QY

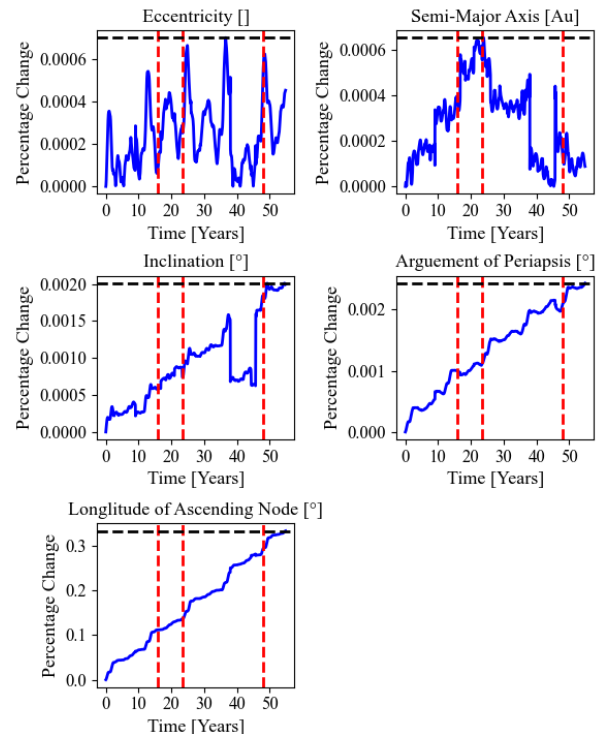


FIG. 62: The fractional change (orange) in the orbital elements of 2008 QY defined on the 12th November 2023 over 20,000 days with days of closest approaches to Earth marked (dashed red) and the maximum fractional change (dashed black)

3. 1999 SL5

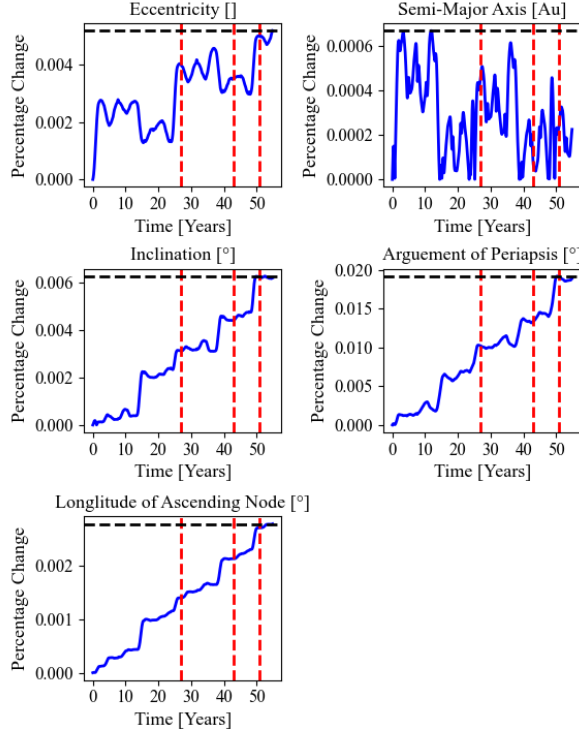


FIG. 63: The fractional change (orange) in the orbital elements of 1999 SL5 defined on the 12th November 2023 over 20,000 days with days of closest approaches to Earth marked (dashed red) and the maximum fractional change (dashed black)

4. 2001 XR31

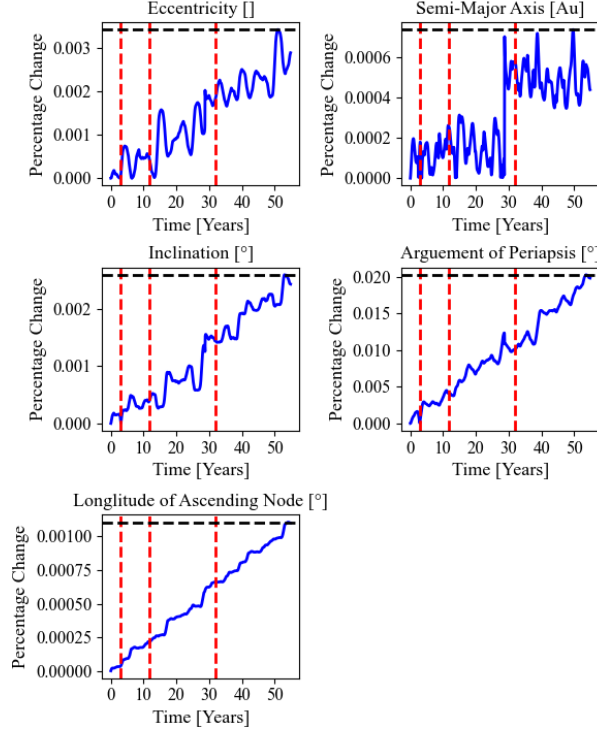


FIG. 64: The fractional change (orange) in the orbital elements of 2001 XR31 defined on the 12th November 2023 over 20,000 days with days of closest approaches to Earth marked (dashed red) and the maximum fractional change (dashed black)

Scientific Summary for a General Audience

Near-Earth Asteroids (NEAs) describe rocky objects in space which pass close by Earth. Although far less common than other types of natural disasters, history shows the devastating consequences that their collisions with Earth could cause. Extreme cases include the 'K-T event' responsible for the extinction of the dinosaurs and half of all life, 65 million years ago. But recent examples, such as the 1908 Tunguska Event, which incinerated 2000 km^2 of Siberian Forest, show how current the hazard is. There is therefore a large ongoing scientific effort to predict future impacts, with the US government signing the George E. Brown, Jr (GEB) Act in 2005 committing to discovering over 90% of near-earth asteroids with a diameter greater than 140 m. The interest in NEAs is not only due to the threat they pose. They also offer an insight into the formation of our solar system and even life on Earth as well as potential mineral-rich mining sites as the depletion of Earth's supply accelerates.

In this paper, we predict the future positions of asteroids by determining their orbits around the sun from a small number of observations taken over a short period of time. This allows us to compare the asteroids and the Earth's orbits to see how close they could potentially come to one another and whether they have the potential to be hazardous. We then map the position of each asteroid relative to Earth over the next 55 years to see when they will come closest. Because we cannot measure the location of the studied asteroids with 100% certainty, and we only observe a very small segment of the overall orbit, we achieve a range of possible orbits from our observations. Therefore, during their closest approaches to Earth, there are multiple different possible positions for a given asteroid. This spread of positions allows us to calculate the probability of a collision with Earth and thus the concern a given asteroid warrants.

We discovered three of our studied asteroids are 'potentially hazardous' due to their size and potential proximity to Earth. Out of all our targets, we find the closest one (2008 QY) will come to Earth is $(6 \pm 4) \times 10^7 \text{ km}$. Although there is a non-zero probability of an Earth impact, it is so small it does not warrant concern. This paper finds we can sufficiently accurately determine the future trajectory of Near Earth Asteroids by observing them for short periods of time, and therefore the methods used could be applied to rapidly assessing the threat and scientific interest of newly discovered asteroids.